Decay of the excited ^{16}O quasi-projectile in the ^{16}O + ^{12}C reaction at 130 MeV

Relatore:
Prof. Mauro Bruno

Correlatore:
Dott. Catalin Frosin

Presentata da:
Maria Vittoria Managlia

Contents

Abstract

Questo lavoro di tesi è stato svolto all'interno del gruppo NUCL-EX dell'INFN. L'argomento della tesi è quello del decadimento di un nucleo eccitato $^{16}O^*$, ottenuto come Quasi-Proiettile in una reazione semi-periferica $^{16}O + {}^{12}C$ a 130 MeV di energia del fascio incidente. È stata effettuata una selezione dei dati che ha consentito di definire una reazione nella quale il nucleo incidente ^{16}O, dopo aver interagito con il bersaglio ^{12}C, si eccita ad energie nell'intervallo $17 \div 22$ MeV, mentre il bersaglio acquista energia cinetica rimanendo nello stato fondamentale oppure si eccita, ma sotto la soglia di energia utile per decadere in particelle. Sono quindi stati considerati i diversi possibili canali di decadimento dell'$^{16}O^*$ e cioè

$$^{16}O \rightarrow {}^8Be_{gs} + {}^8Be_{gs} \rightarrow \alpha + \alpha + \alpha + \alpha \tag{1}$$

$$^{16}O \rightarrow \alpha + {}^{12}C^* \rightarrow \alpha + \alpha + {}^8Be \rightarrow \alpha + \alpha + \alpha + \alpha \tag{2}$$
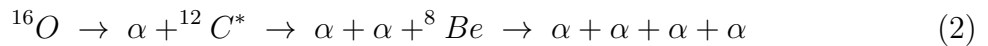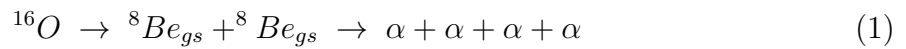
Nel secondo canale sono stati distinti i due casi in cui il $^{12}C^*$ è eccitato nello stato di Hoyle (7.65 MeV) o nello stato 3^- a 9.64 MeV. Per questi canali sono stati considerati, sia separatamente che congiuntamente, i casi in cui il bersaglio rimanga nello stato fondamentale o nel primo stato eccitato γ. Sono state calcolate le probabilità di decadimento nei diversi canali e le energie di eccitazione dell'$^{16}O^*$, che presenta un elevato numero di livelli. I valori ottenuti sono stati confrontati con quelli presenti nei database ufficiali, trovando numerose conferme. Tuttavia, alcuni picchi nell'energia di eccitazione non corrispondono a livelli noti. Ciò può essere dovuto alle indeterminazioni sperimentali, all'interferenza fra livelli diversi o a livelli non ancora determinati sperimentalmente. I dati ottenuti saranno confrontati con programmi di decadimento statistico per poter definire accordi e/o discrepanze per individuare eventuali effetti di clustering, cioè indicazioni di struttura di livelli del $^{16}O^*$ formati da insiemi di 4 particelle α.

Introduction

The decay of light nuclei is one of the active area of research in nuclear physics. In particular, the comparison of experimental data with models, based on the statistical decay, is useful to refine models to reproduce data. On the other side, it is possible to underline discrepancies which cannot be reproduced by models. Indeed, one of the most challenging argument is to understand the importance of clustering effects also in excited state of nuclei. It has been suggested that even-even nuclei can show a structure made of α-particles which manifests in rotational bands at different excitation energies. This has been stated, for instance, for $^{12}C^*$, starting from the first excited state above the threshold for particle emission with rotational bands at higher energies, partially highlighted with experiments. The same should hold for the $^{16}O^*$, but it is not yet experimentally found. In this line, the INFN NUCL-EX collaboration has started a systematic measurements of the reaction $^{16}O + {}^{12}C$ at three different beam energies, i.e. 90, 110 and 130 MeV. This thesis deals with part of the collected data, which correspond to the decay of the Quasi-Projectile $^{16}O^*$ in a final state of 4 α-particles. The number of events available at the two lower energies are not enough to allow for detailed analysis. Therefore, only data at 130 MeV have been analyzed in this thesis. In particular it has been investigated the decay of $^{16}O^*$ in different decay channels, with the Quasi-Target ^{12}C in the ground or in the first excited state. The decay can proceed through the formation of two $^8Be_{gs}$ which both decay in two 4 α-particles, or through one α-particle and a $^{12}C^*$, which can be in the Hoyle state (0_2^+, 7.25 MeV) or in a 3^- excited state at 9.64 MeV. In the different decay channels the excitation energy of the $^{16}O^*$ has been calculated. At variance with $^{12}C^*$, which present the two single levels indicated above, the $^{16}O^*$ presents a huge number of levels in the region available at this beam energy. Some of them are visible in the experimental data and different levels are present in the different decay channels.

In this thesis the first chapter describes the physical context of the work, the second deals with the experimental apparatus and the measurements. The calibration of the data and the analysis are described in the third chapter, together with the obtained results. Finally, some conclusions are drawn together with some perspectives.

Chapter 1

The physical context

The basis of most studies devoted to the understanding of structure and dynamical properties of nuclei is the assumption that nuclei are sets of interacting nucleons. In fact, although nucleons are compounds of quarks and gluons, these remain bound in nucleons and, thus, it makes sense to consider nucleons as the effective elementary constituents of nuclei as long as the considered beam energies are not large enough to excite sub-nucleonic degrees of freedom. From this point of view, the *quantum chromo dynamics* (QCD), which describes the strong interactions between quarks and gluons, can thus also be safely hidden, outside nucleons, in an effective interaction between the nucleons. For this reason, physics of nuclei in the vicinity of their ground state or at low excitation energies is a physics of nucleons interacting via the nucleon-nucleon interaction. This is the case of the present study.

1.1   Introduction to reaction mechanisms

In nuclear physics a nuclear reaction is a type of transformation of matter that involves the nucleus of a specific chemical element which is converted into another with a different atomic number, thanks to the so-called *nuclear forces*. This conversion can include spontaneous changes occurring in the nuclei, known as *radioactive decays*, but also those induced by external means, i.e. through nuclear collisions. These interaction phenomena are due to the impact, also known as *scattering*, between an energetic projectile nucleus (*beam*) and a target nucleus (*target*), generally at rest in the laboratory reference frame. Depending on the purpose and how much one wants to excite the nuclei, the incident beam can be chosen more or less energetic. This way of proceeding allows to access and to study several nuclear properties.

One of the most effective ways to investigate the behaviour of nuclear matter in conditions of extreme density and temperature is the study of the *heavy-ion collisions* in which other nuclei or nuclear composites, possibly short-lived, are produced.

A collision can be classified according to several parameters. First of all there is the relative speed between the two particles before the impact, given by:

$$v_{rel} = \frac{h}{m\lambda_r} \tag{1.1}$$

where m is the nucleon mass, v_{rel} is the relative velocity between the projectile and the target and λ_r is the reduced wavelength related to the nucleon-nucleon interaction. This relative velocity is an index of the available centre-of-mass kinetic energy that can be partially or entirely transformed into excitation energy during the interaction between the two colliding nuclei. Comparing λ_r with the mean nucleon-nucleon distance in a nucleus d_{n-n}, which is $\sim 1.2 \; fm$, two cases can be distinguished:

- If λ_r exceeds d_{n-n}, it can be assumed that the collision process is of a collective nature, since a single nucleon is affected by the average interaction due to the presence of all the other nucleons and not by the single collisions between nucleons. For this reason, the interaction between nucleons inside two colliding nuclei can be explained through the *mean field theory*.

- If λ_r is smaller than d_{n-n}, the binding energy of the nucleons becomes negligible and a two-body interaction is used to explain the process. In this case the target can not be treated as a collective entity.

Generally, the effects of mean field and nucleon-nucleon collisions are always present, but in different proportions according to the case that is being studied.

Another important factor for the classification of a collision is the *impact parameter* which represents the distance between the asymptotic trajectory of the projectile and the parallel line passing through the centre of the target, as shown in figure 1.1.
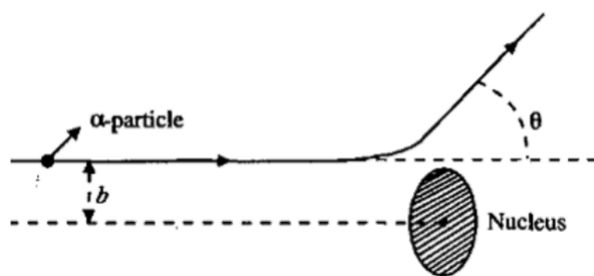
Figure 1.1: Schematic representation of a nuclear collision, specifically an elastic one, between a beam of alpha particles and a target nucleus. b denotes the impact parameter while θ stands for the laboratory scattering angle of the incident particle.

The value of the impact parameter provides information on which interaction mechanisms can occur, as it determines the overlap of the density distributions of the nuclei during the collision.

Let R_b be the average radius of the incident nucleus and R_t the average radius of the target nucleus. Different cases can occur:

- *Electromagnetic elastic diffusion.* In this case $b \gg R_b + R_t$, which means that the strong nuclear force can be neglected since projectile and target are at a large distance. The impact process is therefore governed by the Coulomb field.

- *Grazing condition* where $b \sim R_b + R_t$. The two nuclei come into contact. The most superficial nucleons of the projectile and the target start to feel the strong force while the inner ones do not interact. This kind of reactions are called *direct reactions*. Small amounts of energy can be exchanged by the most peripheral nucleons. There may also be phenomena of excitation of energy levels and elastic reactions. In this case the reaction products have a "memory" of the starting conditions and their identity. For this reason, in the output channel, there is a fragment similar to the projectile, called *quasi-projectile* (QP), and one to the target, the *quasi-target* (QT).

- *Deep Inelastic Scattering* occurs when $b < R_b + R_t$. The nucleons, as a whole, begin to feel the strong force. This case is characterized by strong transfers of energy, angular momentum and nucleons. This significant dissipation of energy also contributes to excite the QP and the QT.

- *Compound Nucleus Production* occurs in the case where b is small approaching 0. As the impact parameter is so small, the impact is defined as *central* and it can lead to the fusion of the two starting elements. The reaction product is a compound nucleus (CN), a metastable system with a mean life of about $10^{-19} \div 10^{-18}$ s [1]. The evolution of this system no longer depends on how it was produced. Once equilibrium in the distribution of energy and angular momentum is established, the CN decays in two different ways, depending on the type of nucleus, its excitation energy and its spin. On one hand there is *fission* in which the compound is divided into two fragments because of the strong nuclear force and the Coulomb repulsion. On the other hand, there is *evaporation* in which the CN loses its excitation energy by emitting light particles and gamma radiation. The resulting nuclear fragment is referred to as *evaporation residue* (ER).

Figure 1.2 shows the above-described mechanisms schematically, as a function of the impact parameter b.
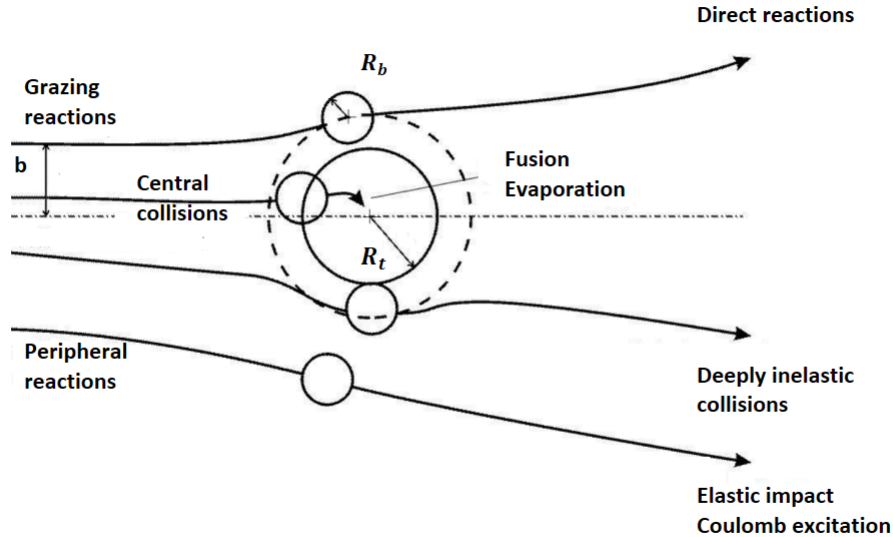
Figure 1.2: Classification scheme of heavy-ion collisions according to the impact parameter.

The impact parameter b is related, in a semiclassical approach, to the angular momentum l of the system by:

$$b = l\lambda \tag{1.2}$$

Hence, the previous subdivision just listed could be done in terms of this quantity. There is an important value of b called the "grazing" impact parameter b_{gr}, which is the minimum value at which nuclear forces are negligible with respect to Coulomb interaction, and there is also a critical angular moment l_{crit}. It separates the processes of inelastic dissipation from those of fusion.

In turn, the angular momentum l is related to the differential cross section for angular momentum units $\frac{d\sigma(l)}{dl}$ by a linear dependence relation, since the geometrical cross section for a given interval $l+dl$ (or $b+db$) is given by $2\pi b db$. The reaction mechanisms associated with the different values of the angular momentum are shown in 1.3. For example, at low energies, l values lower than l_{crit} form the region of central collisions where a compound nucleus (CN) is formed with the complete fusion of the reaction reagents (σ_F). The angular momentum values between l_{crit} and l_{DIC} individuate the region of *Deep inelastic collisions* (σ_{DIC}) and for higher values of l the cross section is dominated by direct "almost elastic" reactions (σ_{qe}).
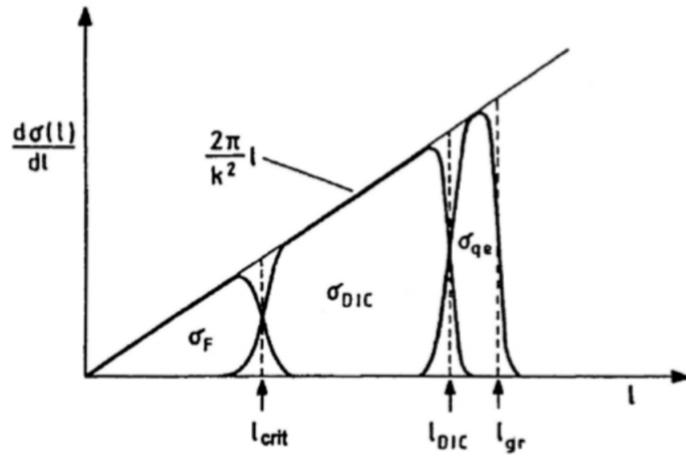
Figure 1.3: Schematic representation, at low energies, of the progress of the contributions to the differential cross section per unit of angular momentum when the angular momentum l varies.

In conclusion, there are two important quantities from a statistical point of view. These are the *total cross section*

$$\sigma = \frac{R}{n_b \cdot \Phi} \tag{1.3}$$

and the *differential cross section with respect to the solid angle*

$$\frac{d\sigma}{d\Omega} = \frac{1}{n_b \cdot \Phi} \frac{dR(\Omega)}{d\Omega} \tag{1.4}$$

where R is the number of particles per unit of volume that have interacted in the unit of time, i.e. the reaction rate per unit of volume, Φ is the ion flow of the beam and n_b is the density of the target nuclei.

1.2 QP excitation in peripheral collisions

In the previous paragraph a classification of the various types of reactions was made according to the values assumed by specific parameters. However, reactions can also be classified by the mechanism that governs the process. As mentioned before, in direct reactions only very few nucleons are involved in the interaction. Specifically, the most superficial nucleons of the projectile interact primarily at the surface of the target nucleus, with the remaining nucleons of both partners serving as passive spectators (figure 1.4).

Such reactions may put or remove a single nucleon from a shell-model state and therefore serve as a way to explore the shell structure of nuclei. These collisions exhaust a large amount of the total reaction cross-section and are thus easily recognized. Among
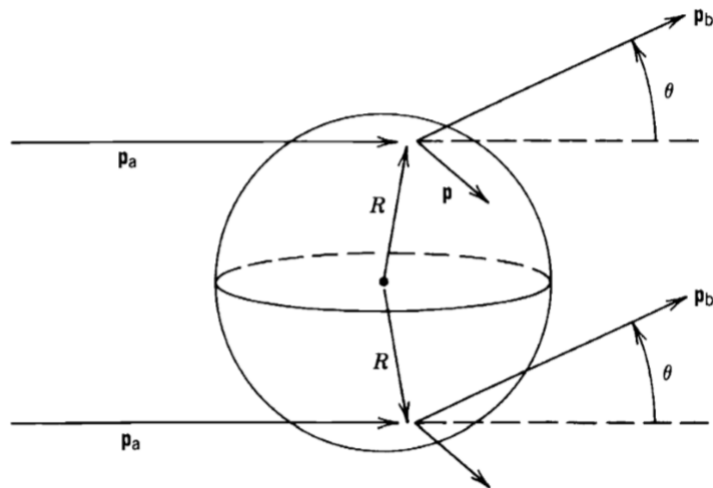
Figure 1.4: Geometry for direct reactions occuring primarly on the nuclear surface. An incident particle with momentum p_a gives an outgoing particle with momentum p_b, while the residual nucleus (target nucelus plus transferred nucleon) must recoil with momentum $p = p_a - p_b$.

them, scattering processes are also included in which the incident and outgoing particles are the same. If the reaction products are in their ground state, the process is called elastic scattering, whereas if they are in an excited state we call it inelastic scattering.

It is well known that in peripheral collisions the two large final products are referred to as *project-like* (QP) and target-like fragments (QT) and are easily recognized in the detectors only if the QP and QT excitation energies are moderate. Several cases can occur due to this interaction between projectile and target. One of the possibilities arises when the QT is not excited, while receiving part of the incident energy by transforming it into recoil kinetic energy. Hence, it remains in its ground state. Another possibility occurs, on the other hand, when the QT takes energy from the projectile and reaches excited states. In both cases QP is in an excited state. Peripheral collisions are, thus, associated with the decay of the excited source QP and/or with the one of QT. Therefore, one can study the decay of the excited QP in reactions in which the QT is in its fundamental or in its first excited states. If the decay chain is complex or long, the final products are quite different from the original QP and QT nuclei. Conversely, if it is simple or short, the QP and QT residues still resemble the initial projectile and target nuclei. As the impact parameter decreases, the relative velocity between QP and QT drops as well as their respective atomic numbers. Finally, for the most dissipative collisions, the notion of QP and QT becomes questionable because most of the emitted matter is in the form of light particles and *intermediate mass fragments* (IMF) [2].

1.3 Clustering effects in nuclei

Even though the shell model, based on a simple independent particle assumption, has been very successful to explain many of the nuclear properties, it was soon clear that not all experimental features could be theoretically predicted . This is also true for the light nuclei which generally represent the benchmark for theoretical models. Contrary to the standard view of a static collection of neutrons and protons in a spherical nuclear droplet, the nucleus is rather a highly dynamic ensemble of nucleons which feature velocities that can reach a significant fraction of the speed of light. In order to minimize the repulsion originating from the Pauli exclusion principle, identical nucleons pair with spins anti-aligned and in orbitals with maximal overlap, leaving a spin-zero entity. This is possible for both pairs of protons and neutrons resulting in a maximally correlated quartet, 2p +2n, known as the α *particle*. This tendency of protons and neutrons to aggregate into discrete structures, called *clusters*, inside the nucleus is referred to as *clustering effect*. These structures have been interpreted in terms of "nuclear molecules". Specifically, this phenomenon can be observed in light nuclei with equal number of protons and neutrons (N=Z). In order to understand these properties, a new viewpoint, other than the independent-particle one, was needed. Starting form the 60's, the prospect that the *molecule-like* structure can appear in wide region of nuclei both in mass number and in excitation energy has promoted an extensive development of theoretical and experimental studies on cluster structure in light nuclei, through several research campaigns.

Clustering behaviour has been seen in a wide variety of ways, including:

- *Magic core plus orbiting cluster.* The valence nucleons, outside a closed shell, can behave like an orbiting cluster, giving characteristic rotational spectra, like those observed for ^{16}O, ^{40}Ca, ^{90}Zn and ^{208}Pb.

- *Very light nuclei.* This case is characterized by small subsystems of the nucleus tightly bound with a tendency for this structure to develop and to be competitive in energy with a mean field configuration. Examples are ^{8}Be $(\alpha + \alpha)$ and ^{12}C (3α).

- *Normal core plus nucleon halo.* The final neutron is extremely weakly bound within the mean field of the nucleus, and its wavefunction tends to extend substantially beyond the edges of the nuclear potential into the classically forbidden region.

- *Large-scale clustering in low-lying levels.* A successful modelling of complex nuclei has been achieved by assuming that they are made up of two mutually orbiting nuclei of comparable masses.

- *Large-scale clustering at high excitation.* The resonances observed at energies close to the Coulomb barrier in heavy ion scattering, particularly between $\alpha-$conjugate nuclei, seem to indicate molecular-like states in which the component nuclei orbit at a distance where they just graze against each other.

- *Complete α-particle condensation.* An extreme form of clustering behaviour is predicted in some models for A multiple of 4 nucleons, wherein the entire nucleus behaves not as one liquid drop but as a condensation into n separate α-like droplets [3]. When extra excitation energy is added to these nuclei the configuration of the mass centres can unwrap and become spatially extended.

In figure 1.5 the wide variety of different types of clustering behaviour is shown.
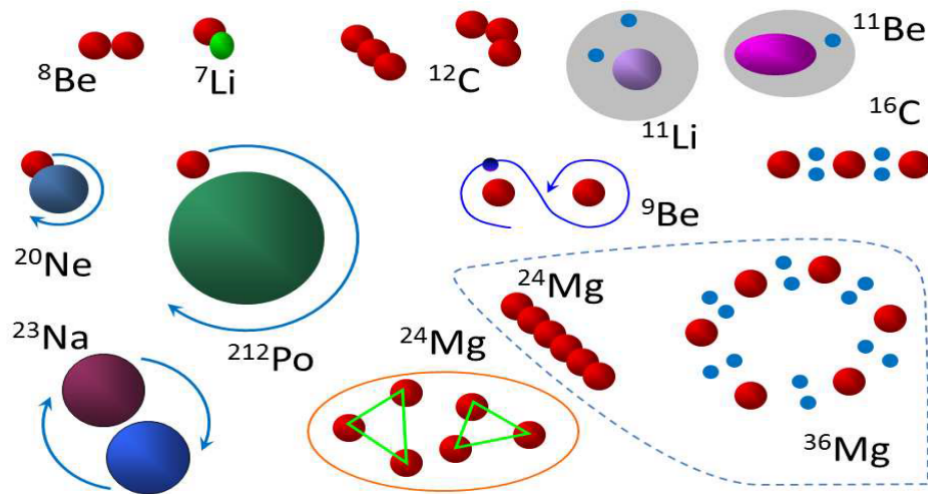
Figure 1.5: Variety of types of nuclear clustering from small clusters outside closed shells, to complete condensation into α-particles, to halo nucleons outside of normal core [4].

The formation of cluster inside the nucleus must be allowed from an energetic point of view. In fact, when the nucleus is separated into its cluster components an energy equivalent to the mass difference between the nucleus and the clusters must be provided. The cluster structure would be expected to be manifest close to the cluster decay threshold and not in the ground state [5].

In order to show the possibility of various kind of nuclear clustering, a diagram was presented for α-nuclei where the molecule-like structure appears prominately. This diagram, referred to as *"Ikeda diagram"*, displays, as a function of energy and mass number, patterns of all kinds of dissociations of α-nuclei at their respective threshold energies. In the original diagram only N=Z were included. In figure 1.6 also neutron-rich nuclei has been included and the diagram extended [5], [6].

The most simple and convincing example of α clustering in light nuclei is the ^{8}Be system. Its ground state is unstable and the nucleus decays into two α-particles with a half-life of $2.6 \cdot 10^{-6}$ s. The ^{12}C element, instead, presents another interesting cluster structure in one of its excited levels. The latter can be thought of as the one obtained by adding another α particle to the ^{8}Be. In 1953, Fred Hoyle postulated the existence

of this excited state of ^{12}C at 7.65 MeV in the attempt to explain the abundance of synthesized carbon in the stars via the triple-α process:

$$\alpha + \alpha + \alpha \rightarrow^8 Be + \alpha \rightarrow^{12} C^* \ [7.65 \ MeV] \tag{1.5}$$
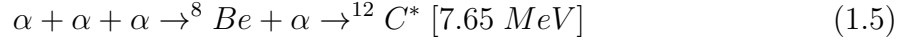
In the boxes on the right and in the center of the diagram in figure 1.6 are shown respectively bound systems with ^{16}O or ^{12}C as a core with bound α particles and neutrons. For example the ^{24}Mg over 14.05 MeV can be described as an ^{16}O core plus two α particles. As for the latter alpha structure, a good example is represented by the nucleus of our interest, namely ^{16}O. This can be pictured above 14.4 MeV as four α particles bound together as one can notice in figure 1.6.
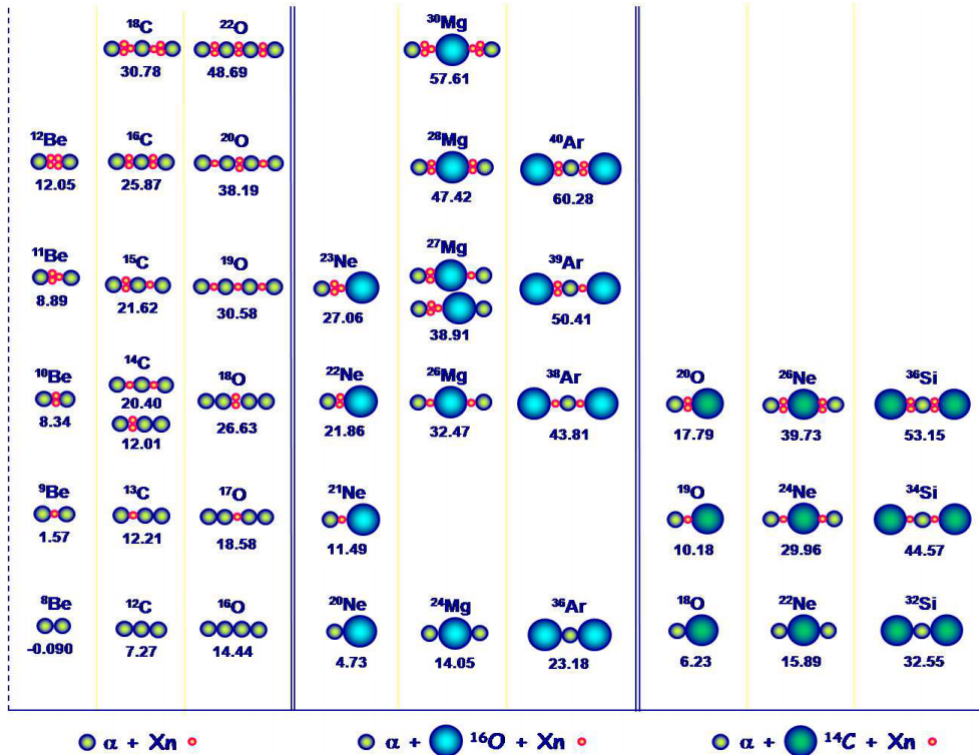

Figure 1.6: The Ikeda diagram which shows the subunits of the possibile molecule-like structure expected to appear next the respective threshold energies for the break-up into subunit nuclei. The threshold energies are written under each structure.

1.3.1 The ^{16}O Nucleus

The aim of the present thesis is the study of the decay of the excited ^{16}O quasi-projectile following a nuclear reaction in which it interacts with a ^{12}C target leaving it in the ground or in the first excited states. For this reason, it is clear that the structure of ^{16}O plays a vital role in this study and it is therefore necessary to spend a few words on it.

The search for clusters-structures, outlined in the previous paragraph, was also aimed at heavier nuclei, such as ^{16}O. For this element several cluster structures have been predicted: at an energy of 7.16 MeV the ^{12}C + α cluster structure and at 14.44 MeV a 4α-structure should be manifest [3]. The latter was suggested by *Chevallier et al.* in 1967 [7]. The study of the ^{12}C(^{4}He,^{8}Be)^{8}Be reaction, carried out by them, suggested the existence of one highly deformed structure whose moment of inertia is approximately four times larger than that calculated for the spherical ^{16}O ground state [8]. In this paper, they have proposed that a structure corresponding to a rigidly rotating arrangement of four α particles may exist in ^{16}O. The ^{8}Be + ^{8}Be decay of ^{16}O has also been studied in a measurement of the ^{12}C(^{16}O, 4α)^{12}C reaction by *Freer et al.* [9]. Although there is a correspondence between some of the observed states by Freer et al., in the reconstructed ^{16}O excitation energy spectrum, and those seen in the work of Chevallier, these last results provide no evidence to support the previously proposed rotational structure consisting of a rigid, linear, arrangement of four α particles in ^{16}O.

Considerable experimental and theoretical effort has been devoted also to the understanding of the mechanism for the disassembly of the excited ^{16}O projectiles into four α particles. For this purpose, over the last few years, several studies were carried out on the possibility of highly excited nuclear matter promptly being fragmented into many pieces. One of the problems affecting the experimental observation of these decay processes was the difficulty of distinguishing prompt decay from sequential decay. Specifically, in the case of ^{16}O, the four α particle exit channels have been investigated. The prompt decay channel of ^{16}O features the immediate disintegration of the nucleus into 4 α-particles, whereas the sequential decay of an ^{16}O projectile into 4 α-particles can take place in two possible ways. The first one, which is the most important one, is the fission of the incident nucleus into two ^{8}Be fragments, each of which later decays into two α-particles.

$$^{16}O^* \rightarrow {}^8Be + {}^8Be \rightarrow \alpha + \alpha + \alpha + \alpha \tag{1.6}$$
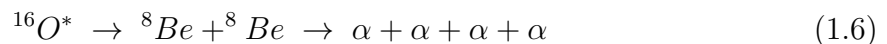
The second one shows an α decay to two different ^{12}C excited states, which then decay to ^{8}Be + α. More precisely, these two excited states are, in energetic order, ^{12}C(7.65 MeV,0_2^+), which is the famous Hoyle state mentioned in section 1.3, and a 3^- state at 9.64 MeV excitation energy [9]. Therefore, this exit channel turns out to be the following:

$$^{16}O^* \rightarrow {}^{12}C^* + \alpha \rightarrow {}^8Be + \alpha + \alpha \rightarrow \alpha + \alpha + \alpha + \alpha \tag{1.7}$$
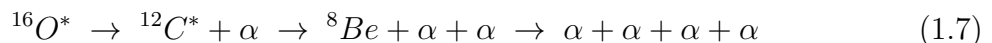
where C* can be the ^{12}C(7.65 MeV,0_2^+) or the ^{12}C(9.64 MeV,3^-) excited state. In some

cases, it might be convenient to use an alternative and compact notation to indicate a nuclear reaction

$$X(a,b)Y \tag{1.8}$$

because it provides information on the common properties of a general class of reactions [2]. This is formally equivalent to the typical notation normally used:

$$a + X \rightarrow Y + b \tag{1.9}$$

where a is the incident projectile, X is the target and Y and b are the reaction products. Usually the heaviest reaction product is indicated with the capital letter. As a consequence, the various decay channels are:

$$^{12}C[^{16}O,^8 Be +^8 Be]^{12}C \tag{1.10}$$

$$^{12}C[^{16}O,^{12} C(0_2^+) + \alpha]^{12}C \tag{1.11}$$

$$^{12}C[^{16}O,^{12} C(3^-) + \alpha]^{12}C \tag{1.12}$$

It is important to highlight that in all the decay channels, either going through the $^{12}C + \alpha$ or two ^{8}Be, the QT can be in its ground state ($^{12}C_{gs}$) or in its first excited state ($^{12}C(2^+)$) as mentioned in section 1.2.

Chapter 2

The experimental apparatus and the measurements

In this chapter the main features and working principles of the experimental apparatus, used to perform the experiment, will be briefly described. The first section is devoted to the description of the G.A.R.F.I.E.L.D. apparatus, only a part of the overall instrumentation, and it is followed by two more detailed subsections about microstrip gas chamber and CsI(Tl) crystals detectors composing G.A.R.F.I.E.L.D. apparatus. Next comes a second section in which, together with the subsections, the *Ring Counter* (RCo) and all its components will be described. The third part of this chapter is focused on the electronics of the whole apparatus and on the data acquisition. A short description of the measurement is done in the last section.

2.1 G.A.R.F.I.E.L.D. apparatus

G.A.R.F.I.E.L.D. is an acronym, which stands for *General ARray for Fragment Identification and for Emitted Light particles in Dissipative Collisions*, for a multi-detector located inside a large scattering chamber at INFN Legnaro National Laboratories (LNL). The G.A.R.F.I.E.L.D. apparatus consists of two large cylindrical shaped drift chambers, one backward, named C_1, and one forward, named C_2, (Figure 2.1), filled at low pressure with CF_4 gas. The two chambers are placed back to back with respect to the target and with the axis in the same direction as the incident beam. An uniform electric field for the drift of electrons and ions, formed along the scattered particle ionization track, is obtained by drift electrodes and a partition cage within the chambers. Each of them has two different types of detectors: microstrip gas chamber pads (MSGC) and CsI(Tl) crystals scintillators.

The forward chamber C_2 is divided into 24 azimuthal sectors, each of which has a MSGC. These are used as the first stage of detection, providing information, from the

ionization of the gas, on the energy loss ΔE by the reaction products, and four CsI(Tl). These last constitute the second stage of detection since they provide information on the residual energy Er of the particles. The C_1 chamber covers the polar angular region between 29.5° and 82.5°.

The backward chamber C_1 has a similar structure to the C_2 with the exception of 3 sectors missing and covers the angular region $97.5° < \theta < 150.4°$. The 45° azimuthal aperture can be used for ancillary detectors

With the combination of these two chambers almost the whole solid angle between $30° < \theta < 150°$, with respect to the beam axis is covered. Considering that every MSGC pad is azimuthally divided in two sub-pads and at the end of each sector four scintillators are placed, there are totally 168 and 192 detection modules, respectively in C_1 and C_2.
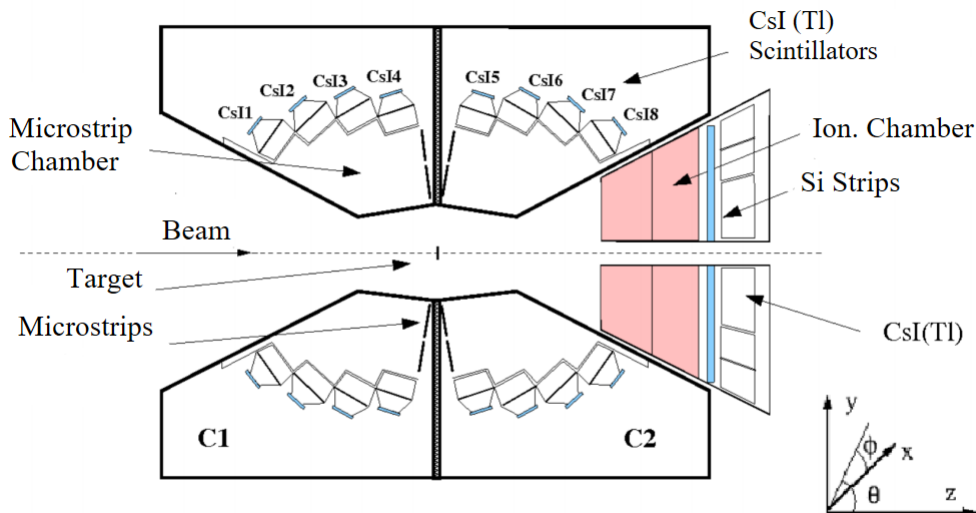
Figure 2.1: Cross section of the G.A.R.F.I.E.L.D. appartus coupled with the RCo. The beam is sent from left to right against the target in the center, between the two chambers C_1 and C_2. In the bottom right-hand corner there is the frame of reference used to pinpoint the different detectors.

Indeed, one of the most important parameters for a detector is the *granularity*, a characteristic which affects the angular resolution and which is related to the probability that two different particles hit the same detector, resulting indistinguishable. This case is known as a *double hit*. In order to reduce the uncertainty on particle trajectories, it is necessary to have a high value of the granularity. This is possible when a large number of detectors is available. As described before, the G.A.R.F.I.E.L.D. apparatus includes 360 detector elements each of which covers an angular range of about $\Delta\phi = 7.5°$ and $\Delta\theta = 14°$ if the chambers are used as ionization chambers. The azimuthal resolution can reach about 1° in combination with the drift time measurement. This consists in

the measurement of the collection time by the microstrip of the produced ionization. In this way, one can have a more precise position measurement.

The whole system is contained in a scattering chamber which is 6 m long and features a diameter of 3.2 m in which high vacuum, of $10^{-5} \div 10^{-6} Pa$, is created. The emptying process takes place in several phases controlled by instruments placed in different positions and with different measuring ranges. This high-vacuum condition is fundamental in order to avoid dissipation of energy in residual gases inside the chamber by the beam. The charge preamplifiers are assembled within the chamber with the aim of reducing the noise from signals, minimizing the cable length and capacity.

Finally, the target, a thin sheet of some material, is placed on an orthogonal mechanical guide with respect to the beam. With a motor system it is possible to change the target and 12 positions are present. At the entrance of the apparatus there are three magnetic focusers that allow the collimation of the beam, coming from the accelerator, on the target.

2.1.1 MSGC microstrip detectors

The operation of the gas chambers is based on the process of gas ionization by a charged particle passing through the gas. Indeed, the particles produced in a reaction, once entered in the drift chambers through the entrance window, interact with the gas. This interaction can lead to either excitation or ionization of the gas molecules. It is in the second process that the electron-ion pairs, which represent the charge carriers, are generated. The number of ionizations (or the number of the pairs electron-ion) depends on the energy needed to extract a single electron and on the energy loss by the charged particle or fragment. The number of the produced electrons is proportional to the energy loss ΔE.

As already mentioned, inside the chambers an electrical field is generated thanks to a drift cathode at around -1000 V, a Frisch grid at 60 V and a field cage. The electric field is oriented in such a way that the electrons, formed along the trajectory of the particles, are forced to drift toward the microstrip pads. It is very important that the electric field is as homogeneous as possible in order to have a constant drift velocity for the electrons, obtaining straight trajectories, so that from the drift time one can deduce the flight path of electrons knowing a reference time, for istance the time the particle reaches the scintillator. Typical values of electric field inside the G.A.R.F.I.E.L.D. chamber are of the order of $10^4 V/m$. The Frisch grid, which is placed at 3 mm from the microstrip plane, delimits the region in which the drift field is very intense, about $10^7 V/m$ [10], from the one in which the electrons simply drift towards the electrodes, since the electric field is weaker. Near the microstrips, electrons undergo a sudden acceleration, thus starting the multiplication effect, know as *avalanche effect*. The final number of electrons is proportional to the number of electrons generated by the ionization, in this allowing to measure the energy of the particles weakly ionizing the gas. This reduces the minimum

detected energy to less than 1 MeV/u.

The microstrip pads (Figure 2.2) have a particular trapezoidal shape, specially designed, and they are arranged almost perpendicular to the beam axis ($85°$ in θ) and they are equipped with alternated metal cathodic and anodic electrodes. Each pad is divided both longitudinally and transversely, thus identifying four charge collection areas, named conventionally 1A, 1B, 2A and 2B. Looking at the glass pads with the small base downward, the letters A and B indicate respectively the left and right sides, while the numbers 1 and 2 refer to the nearest and furthest halves from the beam.
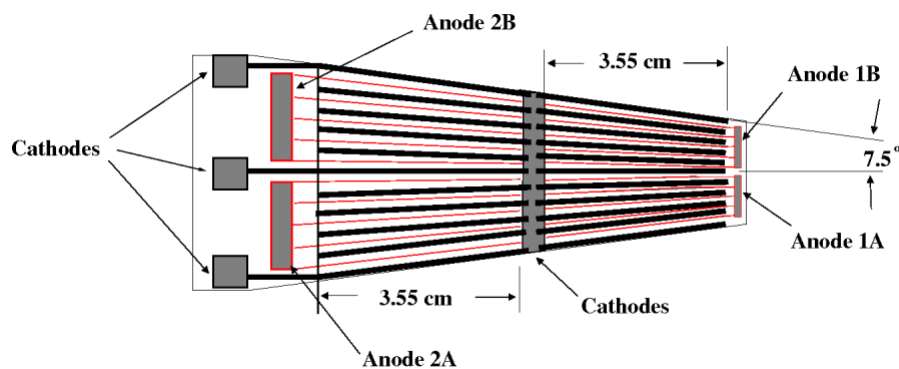
Figure 2.2: Schematic representation of a microstrip pad belonging to the G.A.R.F.I.E.L.D. apparatus. The division in the four charge collection areas is clear.

All the cathodes are grounded, whereas the anodes are electrically connected to the four zones and biased at $430V$ [10]. The division into two longitudinal sections helps to get a higher precision on the azimuth angle, while cross-sectionalization provides an additional stage of detection. This system, together with the scintillators, allows the realization of a $\Delta E - E$ correlation for the identification of particles.

The choice of using microstrip gas as detectors is convenient for several reason. The request of energy threshold as low as possible is satisfied with the capability of detecting particles with very low energies. Furthermore, MSGC have the advantage of maintaining a wide dynamic identification range and, at the same time, of having a high signal-to-noise ratio for low ionization ions. Microstrip chamber, in fact, allow high counting rate and high gains. Moreover, the drift chambers make it possible the measurement of the direction of the particle track.

2.1.2 CsI(Tl) crystals scintillators

A scintillator is a material that is able to emit light as a result of the excitation of their atoms due to the crossing of a charged particle. The crystals are doped in order to increase the light emission efficiency of the scintillator, to reduce the self-absorption

and to have the desired wavelength of the output light for an optimal matching with a photodiode (Figure 2.3).
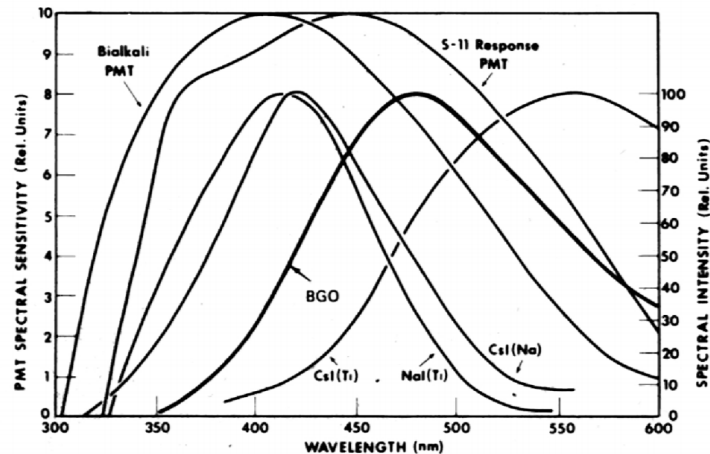

Figure 2.3: Emission spectra of different scintillators and absorption spectra of photodiodes. For the proper functioning the superimposition has to cover all the emission spectra of the scintillator.

In this case a thallium doping, of about 1200 ppm, is employed [10]. To avoid possible loss of the produced light and in order to shield them from the outside, the crystals are wrapped in a white diffusive paper and covered by a layer of aluminated *mylar*. With the chosen diffusive wrapping, this doping contributes to maximize the light collection.

As already mentioned, each G.A.R.F.I.E.L.D. sector contains four CsI(Tl) scintillators, the shape of which has been designed in order to optimize the geometrical efficiency. 96 crystals are present in the forward chamber and 84 in the backward. Each detector covers $\Delta\phi = 15°$ and $\Delta\theta \simeq 15°$. The crystal thickness is 4 cm in order to stop the charged products expected in the energy range of interest. The CsI(Tl) crystals are optically coupled to Hamamatsu S3204-05 photodiodes which are in turn connected to the pre-amplifiers. The energy resolution of CsI(Tl) is about 3% for 5 MeV α particles and $2 - 3\%$ for 8 MeV/u Li and C elastically scattered beams on Au target [10].

The operation of scintillators (Figure 2.4) is based on the fact that one of its atoms can be ionized or excited due to the interaction with a charged particle. The conduction band of the scintillator is composed by electrons free to move and the valence band consists of the less bound electrons of the atomic shell. If the electrons acquire enough energy, one has two possibilities: they pass in the conduction band forming electron-hole couples or they do not reach the conduction band creating holes with *excitons*, a state in which the electron is electrostatically bound to the hole. In both cases, the de-excitation of the electron occurs when this last recombines with the hole.

The emission spectrum of the scintillator is given by the sum of two exponential
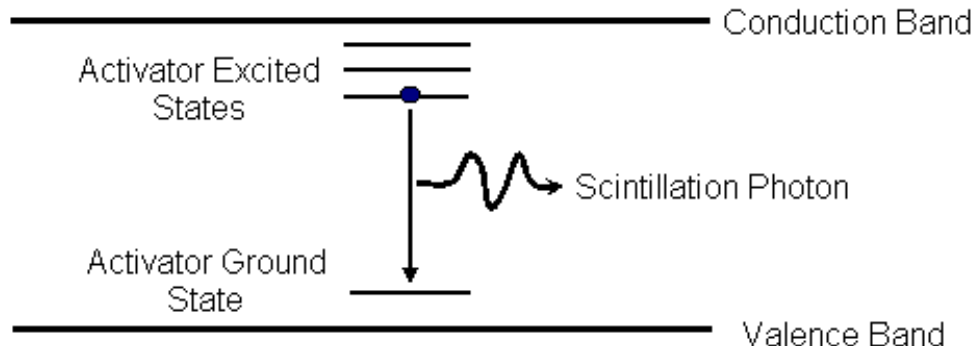
Figure 2.4: Scheme of the scintillation process in an inorganic scintillator, such as CsI(Tl) crystals.

terms with different decay times: a short one ($\tau_s \sim 0.75~\mu s$) and a long one ($\tau_l \sim 5~\mu s$), generally called *fast* and *slow* components. As a result, the current pulse produced in the photodiode by the scintillation light can be described by:

$$i_l(t) = \frac{dQ_L(t)}{dt} = \frac{Q_s}{\tau_s}e^{-\frac{t}{\tau_s}} + \frac{Q_l}{\tau_l}e^{-\frac{t}{\tau_l}} \tag{2.1}$$

where $Q_L(t)$ is the whole collected charge at time t; Q_s and Q_l are the charges produced respectively by short and long components of scintillation. Q_L is thus given by:

$$Q_L = \int_0^\infty \frac{dQ_L(t)}{dt}dt = Q_s + Q_l \tag{2.2}$$

The fast and slow components depend differently on ionization density, therefore on the mass, energy and charge of the incident particle. This property allows to distinguish the mass of the ions from an analysis of the impulse form, a technique called *pulse shape analysis* (PSA) [10], [11].

2.2 Ring Counter

The Ring Counter (RCo) is a three-stage annular detector with a truncated cone geometry. It has the function of identifying and detecting particles by means of PSA and the $\Delta E - E$ telescope techniques. It is placed at the exit of the forward chamber, as shown in Figure 2.1, and it is designed to be centred at $0°$ with respect to the beam direction. It covers the polar angle in the range $5° < \theta < 17.0°$. The Ring Counter has a cylindrical symmetry along the beam axis and it is divided into 8 azimuthal sectors each one with $\Delta\phi = 45°$ angular coverage.

The first stage is an ionization chamber (IC), followed by a strip silicon detector (Si) while the last stage is formed by CsI(Tl) scintillators. In particular, each sector of the Ring Counter is composed by one IC, one silicon *pad* segmented in eight *strip* and six 4.5 cm thick CsI(Tl) crystals. So altogether, there are 48 Cesium Iodide crystals, each one covering half sector in the azimuthal coordinate (Figure 2.5).
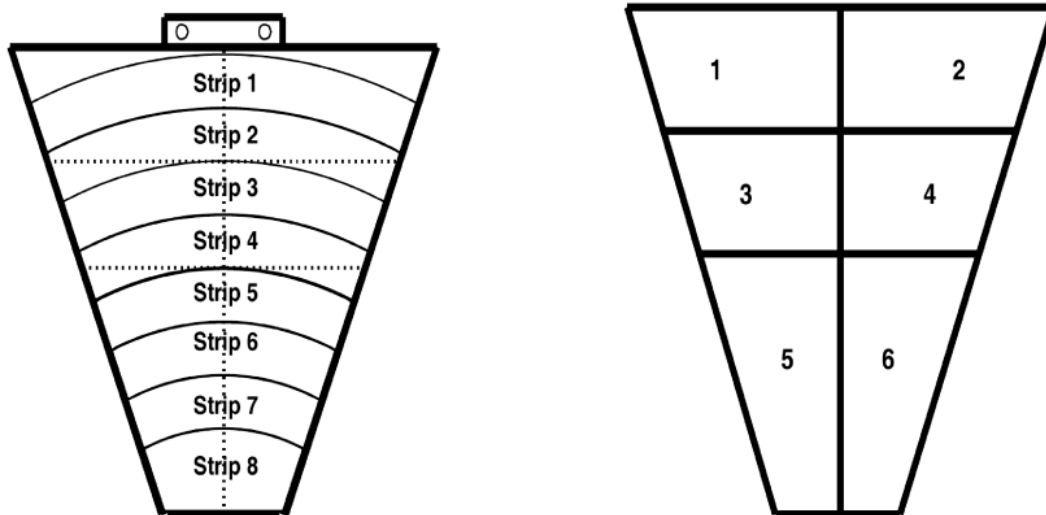
Figure 2.5: The Ring Counters silicon strips (left) and the superposition (right) with the corrisponding Cesium crystals. It can be seen that at least two silicon strips correspond to each crystal.

As a result of the mentioned division in sectors, an accuracy of 22.5° is obtained in the azimuthal angle of the particles impinging on the scintillators. These CsI(Tl) crystals can also reach an overall $2 - 3\%$ energy resolution.

A remotely controlled collimator system has been implemented in order to apply different screens in front of the RCo under vacuum and, therefore, while running the experiment. The screens are used for focusing, shielding or collimation purposes. The RCo is installed on a sliding aluminum support and can be remotely moved back and forth in order to replace the front collimator.

2.2.1 Ionization chamber (IC)

The IC is designed with the aim of optimizing the geometric efficiency, minimizing the active losses of the area. For this reason, its *dead zone* coincides with the one of the silicon detector of the second stage. It is 6 cm long and contains three electrodes of aluminized *mylar*: an intermediate 1.5 μm thick anode and two grounded entrance and exit cathodes of thickness of 3 μm . The ionization chamber of the RCo does not contain

any Frisch grids and the drift field has axial direction. This configuration has been chosen in order to obtain the same reduced electric field by applying half the voltage that would be needed in the absence of the intermediate anode. Furthermore, the high voltage electrode is completely inside the gas volume, whilst the others are grounded, minimizing, in this way, discharges to surrounding materials. As already stated, this chamber is filled with CF_4 since this gas has a high density (0.19 mg/cm^3 at a 50 mbar pressure and at a temperature of 20° [10]) and, therefore, an high *stopping power*. Thanks to this property, the gas can be kept at a relatively low pressure, while having a sufficient energy loss for identification. The gas is continuously cleaned flowing inside the chamber maintaining the pressure constant through a remote control valve; before entering, the gas is filtered to remove residual oxygen and water vapor.

2.2.2 The silicon detectors

The silicon detectors used for the RCo are made using nTD (*neutron Trasmutation Doped*) silicon type which has a better doping uniformity compared to the silicon normally used. An uniform doping allows to reduce the dependence of the induced signal shape by the ion incidence point. In this way, better identification performance from signal pulse shape analysis can be achieved. The silicon detectors have been reverse mounted [12], so that the particle enters through the low field side in order to enhance the pulse shape discrimination capability [13].

Each of the 8 sectors contains a 300 μm thick silicon pad segmented into 8 *strips*, as shown in Figure 2.5. In this figure one can also see the dotted lines corresponding approximately to the overlap with the different CsI(Tl) crystals behind the strips. Each pad covers a solid angle of $2 \div 6$ msr and is completed by a *guard ring*, mounted all around the strips and properly biased, which is needed to minimize the field distortion effects in the inter-strip regions (220 μm wide). The active area of these detectors constitutes 90% of the total area. The inactive area corresponds to the space for the support of each detector and the space between the strips, containing the guard rings. In this way, the charge carriers splitting and *cross- talk*, the signal coming from contiguous strips, are almost negligible. Regarding technical characteristics of the detectors, the bulk resistivity of the detector is of the order of $3400\Omega \cdot cm$, and the full depletion voltage is 100 V with recommended bias of 120 V. The reverse current of each strip is about 30 nA [10].

2.2.3 CsI(Tl) scintillators

The third and last stage of each sector, in which the RCo is divided, consists of 6 CsI(Tl) scintillators. The 4 Si *inner strip* polar angular region is azimuthally covered by 2 of these crystals with $\Delta\phi = 22.5°$ each, whilst, the 4 *outer strip* region is covered by 4 scintillators, each covering half of the polar and half of the azimuthal range defined by the strips (Figure 2.5). The small size of the crystals allows a more uniform doping and, therefore,

better scintillation response and collection of light of the single detector. As a result, there are altogether 48 scintillators, 45 mm thick, which have been optically coupled with Hamamatsu S2744-08 photodiodes with active area 10×20 mm^2. The present CsI(Tl) crystals have been chosen with a Tl doping in the range of $1500 - 2000$ ppm as to enhance their light output and therefore they can reach an overall $2 - 3\%$ energy resolution [10]. The pre-amplifiers are the same used in G.A.R.F.I.E.L.D.

2.2.4   Monitor detector

At a very small angle ($\sim 1°$), a plastic scintillator is positioned inside the scattering chamber to allow the counting of elastic scattering events by Coulomb potential, known as *Rutherford collisions*. The exact location of the plastic detector in the chamber is of great importance since there is a strong dependency of the cross section from the angle

$$\sigma_{Ruth} \propto \frac{1}{sin^4(\frac{\theta}{2})} \tag{2.3}$$

These counts are used to normalize the measurements of the other detectors, namely to obtain an absolute cross section once the Rutherford cross section at that angle θ is known.

2.3   Electronics and acquisition

The electronics of the G.A.R.F.I.E.L.D. and RCo apparatus is used to collect the signals coming from the detectors, through pre-amplifiers with different gains, and to reprocess stored information. For all the detectors used, the deposited energy by the particle in the active volume produces a current pulse in the reading circuit. The charge associated with this pulse is proportional to the incident energy itself and it is obtained integrating the pulse into the *charge preamplifier*. The output signal is then processed by an appropriate electronic chain. In order to minimize noise influence upon the small signals generated, the preamplifiers are located inside the scattering chamber.

The signals of the whole RCo and CsI(Tl) crystals of G.A.R.F.I.E.L.D. are digitized by means of an *Fast Sampling Analog-to-Digital Converter* (ADC). Subsequently, they are analyzed by the *Digital Signal Processor* (DSP) which is programmable and it allows to carry out an advanced on-line data reduction and elaboration. This means that only filtered data, by applying shaping algorithms, are considered instead of sending all the digitized samples to the acquisition. The DSP is useful because relevant physical quantities can be derived, such as amplitude and rise time of the charge signal. However, so as to check the behaviour of the cards, every 1000 events the DSP sends a complete waveform to acquisition for further off-line checks and debugging analysis. The information extracted, expressed in numerical form, are stored into files for the analysis.

The output values of the ADC are continuously recorded in an internal FIFO (*First In First Out*) memory that stores up to 8192 samples, that is approximately $\sim 64 \ \mu s$ at 125 MSPS ($125 \cdot 10^6 \ samples/s$) [12]. This kind of memory acts as a circular *buffer* and the first locations are continuously rewritten in the meantime that a trigger signal arrives which entails the beginning of the process of data recording.

On the other hand, the microstrips signals of the drift chambers are treated with analog electronics which is composed of a charge amplifier followed by a *peak sensing* ADC.

In figure 2.6 the structure diagram of an acquisition channel is shown. Observing the scheme, the input stage of the analog signal, the digitization section (ADC), the temporary FIFO memory, the trigger section and the DSP are distinguishable.
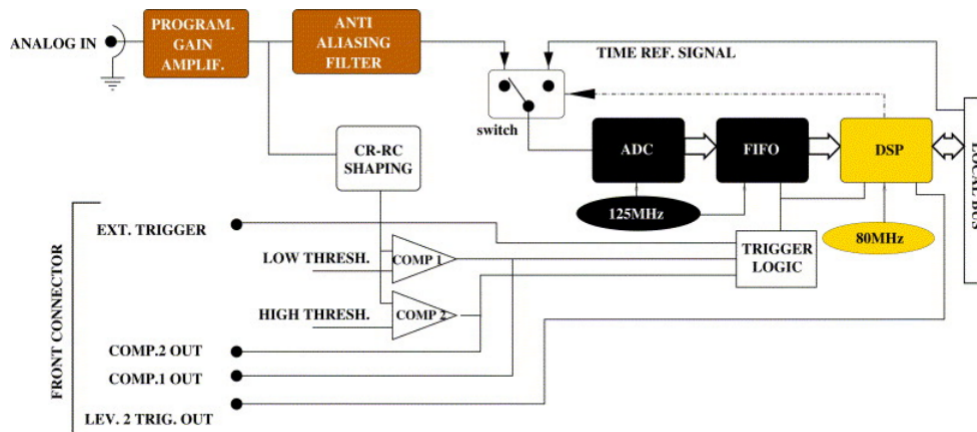

Figure 2.6: Main components of a digital acquisition channel.

2.3.1   Trigger system

In the schematic diagram of figure 2.6 a section called "trigger logic" is present. Basically, the *experiment trigger* is a logical signal produced when an event of interest occurs. Therefore, the choice of the particular trigger logic to be used is crucial for each experiment as this is closely related to reaction mechanisms to be studied. In other words, the trigger represents a direct connection with the physics of the reaction. In this way, particular physical conditions are imposed using logical combinations of trigger signals. If everything coming from the detectors was acquired most of the data would be useless because they represent events mostly dominated by the elastic and quasi-elastic rates.

There are two different kinds of triggers used for these selection: the *local triggers* and *validation signals*. The former are generated from a detector signal that has exceeded its acquisition threshold by means of a *Constant Fraction Discrimination* (CFD). So

that, it is possible to obtain local triggers from the CsI(Tl) crystals of G.A.R.F.I.E.L.D. or from the RCo silicon detectors. The latter are generated by sending the elementary signals, necessary to produce the trigger, to a card VME (CAEN V1495), referred to as *trigger box*, which by the means of a *Field Programmable logic array* (FPGA) produces not just one, but several experiment triggers. When one of the experiment triggers is accepted, the trigger box produces a validation signal that enables the acquisition and the memorization of the signals of all the hit detectors.

During the experiment, it is possible to enable all or part of these triggers, and for each of them to set a reduction factor or exclude it completely. The electronics of the apparatus is equipped with 8 different possibilities of triggers, each associated with a different logic as shown in the table below (table 2.1).

Bit	Trigger	Reduction	Description
0	OR CsI GARF	2	OR of the GARFIELD scintillators
1	OR IC RCo	1	OR of the different parts of IC
2	OR Si RCo	1	OR among the RCo strips
3	OR GARF AND OR Si RCo	1	AND of trigger 0 and trigger 2
4	OR GARF AND OR IC RCo	1	AND of trigger 0 and trigger 1
5	OR Si AND OR IC	1	AND of trigger 2 and trigger 1
6	Plastic Monitor	100	Plastic Scintillator
7	Pulser	1	Pulse Generator

Table 2.1: The available triggers with their mostly used reduction factors.

The trigger output is a bitmask that indicates which trigger is activated. The reduction factor "X" is useful because it activates the data acquisition once every "X" occurrences. The OR signal is activated when at least one detector has produced a signal; the AND signal only when at least two different detectors have produced a signal at the same time. In this way, the OR of a class of detectors allows to analyse the events in which at least one particle has been detected. On the other hand, the AND triggers allow to study events in which there are at least one particle in one set of detectors and one in another. Finally, the multiplicity triggers n allow to study events in which n particles have been detected by a type of detector. Throughout this experiment, the triggers selected are trigger 0, OR of triggers coming from the G.A.R.F.I.E.L.D. signals, and trigger 2, OR of trigger signals from the RCo (table 2.1). More specifically, trigger 0 is the logic OR of all CsI(Tl) signals while trigger 2 is obtained from the logic OR of Si strip signals. These triggers are determined based on the two types of reactions. We are interested in studying mainly fusion-evaporation or projectile decay mechanisms. Both are characterized by having to detect light particles or heavier fragments with similar kinematics. In addition to the measurement triggers mentioned above, two other triggers are used. The first is trigger 7, a pulser trigger, which control the stability of the whole

electronic chain. This is especially useful when interested to sum data from several runs of measurement. The last is trigger 6 which is referred to the plastic scintillator.

In figure 2.7 the logic array of the trigger box is shown as displayed on the acquisition program screen.

Figure 2.7: The logic array of the *trigger box*

The rows indicate the 8 different triggers, while the columns represent the detectors. The green boxes show the logical connections made. Note that in this figure the CsI(Tl) sectors of G.A.R.F.I.E.L.D. and Si strips of RCo are marked respectively in the first and third raw. Indeed, they correspond with the triggers used during the measurement. The blue boxes represent the NOT logic operation of two OR links used for the construction of the AND.

2.4 The measurement

The measurements were performed at the INFN laboratories in Legnaro using a pulsed beam of ^{16}O with an energy of 90, 110 and 130 MeV available using the Tandem XTU accelerator. The ^{16}O produced beam, in this acquisition session, features a maximum intensity of about 0.1 pnA and impinges on a ^{12}C target which is 85 $\frac{\mu g}{cm^2}$ [1] thick.

If the same target is subjected to continuous collisions it may wear out or degrade, leading to a variation of the cross section and of the possibility that the reaction takes place. It follows that a target replacement is necessary, from time to time, in order to maintain the reaction parameters unchanged. For this reason, it is possible to change the target through an automated system which avoids opening the chamber and wasting time in the emptying and filling processes. During the measurements, a set of triggers was used in order to select, already in the acquisition phase, the events of interest. As mentioned in section 2.3.1, the triggers used throughout this experiment were the

---

[1]Making the ratio between the unit of measurement used and the volumetric density of the element the thickness of the lamina expressed in *cm* is obtained.

signals coming from the logic OR of all CsI(Tl) and of all Si strips of the RCo. In order to provide a reference point for the energy calibration also the $^{16}O + ^{197}Au$ elastic scattering reaction has been performed.

Before starting the experiment it is important to check if the beam is centred with respect to the position of the target to which the detectors are referred. For this purpose, an additional AlO_2 target is present in the target holder. This material has the property of emitting light when it is hit by the beam and the target features a centred little hole, corresponding to the calibrated position of the origin. This system, with two other AlO_2 foils placed at the beginning and at the end of the scattering chamber, allows to check the beam alignment and to control its size to about 1 mm in diameter.

An online control of the functioning of the overall apparatus and of the acquired data during the measurement sessions is possible thanks to a graphical interface program named G.A.R.F.I.E.L.D. Monitor [14]. This software enables to visualize several pre-defined 1D and 2D histograms filled either with raw experimental data or with pre-processed variables. An example of these histograms are graphs shown in figure 2.8.
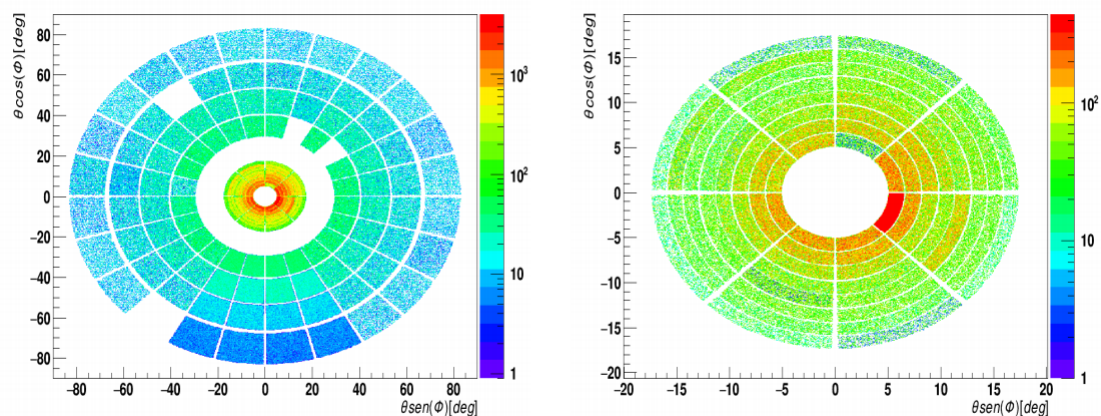
Figure 2.8: Countings for the complete apparatus (G.A.R.F.I.E.L.D. + RCo) on the left and for the Ring counter on the right. It should be noted that in G.A.R.F.I.E.L.D. four detectors are not counting due to bad functioning [15]

In 2.8 the colour of each detector is proportional to the number of events and, therefore, the presence of a small number of events is related to detectors turned off because deactivated or malfunctioning. Finally, in order to verify the stability of the electronic chain, it is possible to acquire *pulser* runs. A pulser is an electrical pulse at different voltage, but similar in shape to that coming from the detectors on the pre-amplifiers. Acquiring this type of measures enables to test the stability and linearity of gain and to verify if they are sensitive to environmental conditions.

Chapter 3

Data analysis and results

In the first part of this chapter, the energy calibration of the data and the methods, $\Delta E - E$ and Pulse Shape Analysis (PSA), used to identify the particles detected with the G.A.R.F.I.E.L.D + RCo apparatus are described. Then follows a part in which few global observable and the ways in which they are selected for particular reaction mechanism of interest are present. Finally, the last sections are devoted to the description of the various analyses carried out only on data at 130 MeV, since the number of events available at 90 and 110 MeV beam energy are not enough to allow for a detailed analysis.

3.1 Energy calibration

The energy calibration of the detectors of the entire apparatus represents one of the crucial points in all the data analysis. It provides the energy value in eV for all the particles detected during the reaction.

For detectors, such as RCo silicon strips, whose response is linear with the energy deposited, an energy calibration has been performed by carrying out elastic scattering measurements of a ^{16}O beam on a sheet, $\frac{200\,\mu g}{cm^2}$ thick, of ^{197}Au. The measurements are carried out in two separate phases: in the first one the ionization chamber is filled with gas, while in the second the chamber is empty. For the measurements without gas, signals coming from the silicon detectors correspond to the energy values calculated from the Rutherford expression for the elastic scattering [1]. By fitting these experimental points, it is possible to obtain a curve that best approximates the relation between the height of the signals supplied by the instrumentation and the calculated energy. The scattering measurements carried out with gas should confirm the validity of the previous energy points (130 MeV). In this case, the calculated energy values are obtained by subtracting the energy loss which occurs in the first stage due to the presence of a layer of gas before

---

[1]The energy loss of the beam in half of the target has been subtracted to the beam energy. In addition also energy loss of products in the second half of the target has been taken into account.

the Si strip detectors. In the case discussed, what is expected is that the signals in electronic channels are linearly proportional to the energy of the diffused particle and stopped in the individual detectors. Indeed, what is observed in the calibration energy curve (figure 3.1) is a linear trend of the experimental points. The absence of non-linear effects implies that there are no electronic non linearities.

As far as the CsI(Tl) crystals are concerned, whose response in *Light-Output* (LO) is not linearly proportional to the energy deposited in the detector, it is not possible to have a simple conversion factor from the LO to the deposited energy. At equal energy detected, a dependence of the interacting ion on the charge Z and on the mass A is found. From measurements carried out to investigate the CsI(Tl) response, the NUCL-
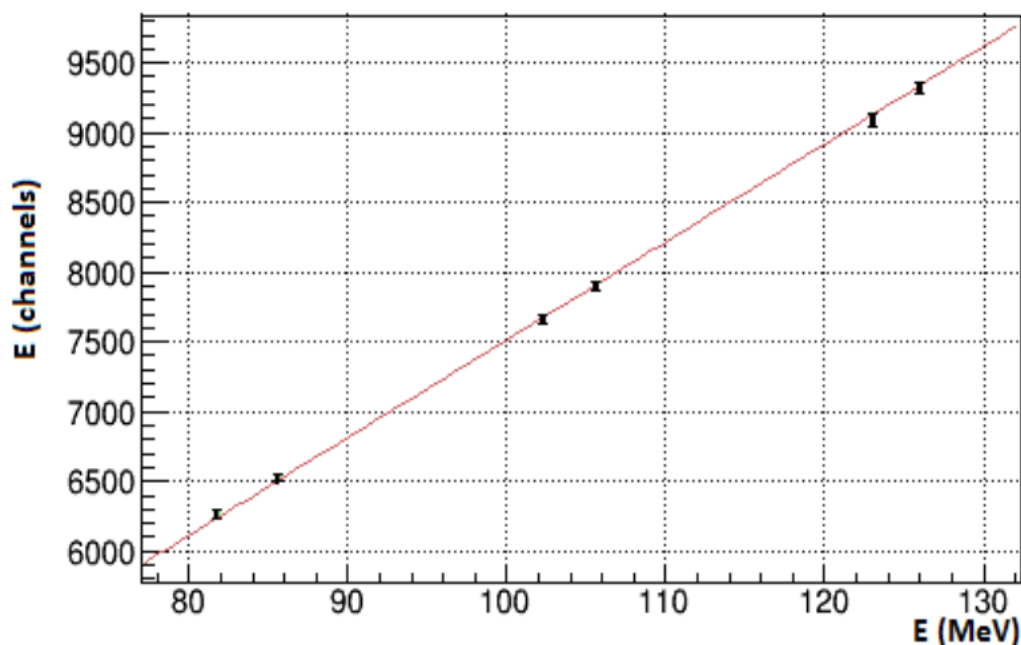
Figure 3.1: Fit procedure on the elastic scattering points, in the presence and absence of the gas in the IC, for strip 5 in sector 3 [16].

EX collaboration has deduced a semi-empirical formula to express the relation between the amplitude in channels of the LO and the energy deposited by the particle when Z and A vary. The formula is the following:

$$LO(Z_{eff}, E) = (d_1 + d_2 e^{-d_3 Z_{eff}})(1 + d_4 Z_{eff})E^{d_5 - d_6 exp(-d_7 Z_{eff})} \qquad (3.1)$$

where the $Z_{eff} = (AZ^2)^{1/3}$ factor takes into account the dependence of LO on the atomic number and the mass number of the incident ion, whereas the d_i parameters with

$i = 1..7$ were set by means of elastic diffusion measurements with ion beams from Z=1 to Z=28 [17]. For the calibration, it is assumed that the uncalibrated light response of the CsI, as obtained from the acquisition system, follows the expression (3.1) with the only exception of a multiplicative factor. In order to obtain this factor, called β-factor by the collaboration, the ratio between the theoretical value for a set of known ions and energies derived by applying the formula (3.1) and the experimental amplitude value is calculated. This is possible, indeed, because a sample of known energy events is available. Although eq. (3.1) has been derived for G.A.R.F.I.E.L.D. CsI(Tl) crystals, it can be applied also to the RCo scintillators. However, in this case, the elastically diffused beam ions fail to reach the scintillator due to the presence of silicon layers interposed. For this reason, a different calibration procedure must be applied. Since the silicon strips have already been calibrated in energy, the amount of energy lost in the silicon of each ion that reaches the CsI(Tl) is calculated. When the crossed thickness are known, it is possible to calculate the value of the deposited energy in CsI(Tl).

Finally, the measured LO value is correlated with the corresponding value calculated through the (3.1), thus obtaining a distribution of the points as the one shown in figure 3.2.
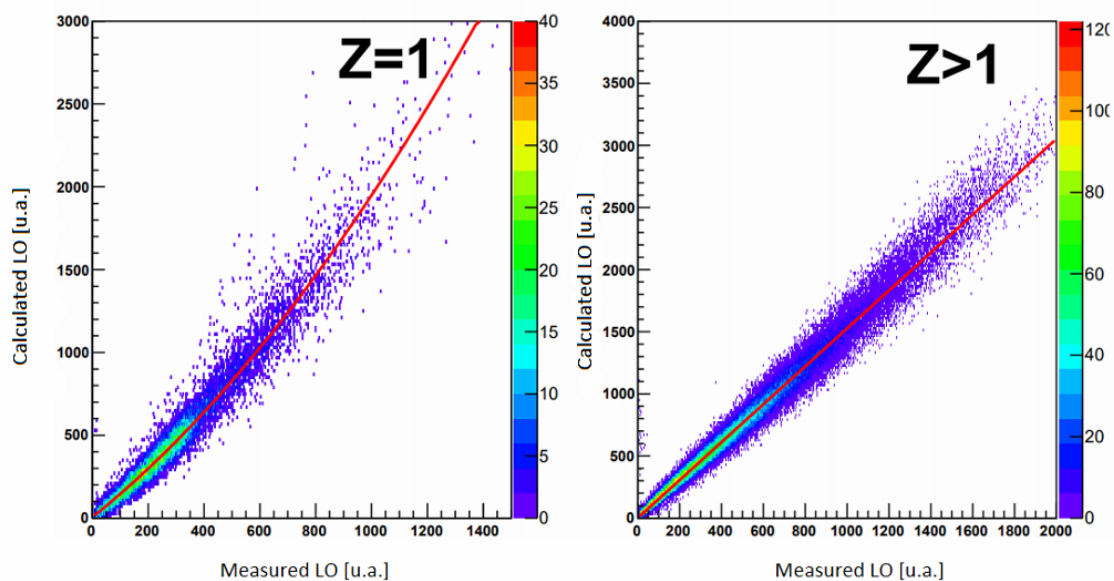
Figure 3.2: Correlation *LO calculated vs LO measured* for RCo CsI (Tl) crystals. The distribution for $Z = 1$ was fitted through a parabola while for $Z > 1$ with a straight line. The parameters returned by the fit correspond to the β-factors for the RCo [18].

3.2 Identification of detected ions

As mentioned in section 2.3, the electronics of the G.A.R.F.I.E.L.D. and RCo apparatus is used to collect the signals coming from the detectors and to reprocess stored information. The collected data are arranged in a collection of "raws", each of which represents an event and features a list of acquisition data parameters characterized by the same event number. These parameters include energy, speed, charge and mass of reaction products and the identification number of the detector hit by the particle to get information on the emission direction. By studying all these parameters it is possible to reconstruct the dynamics of the interaction and recreate the characteristics of the particles from the detectors signals. It is therefore evident that the identification of the particles produced in an interaction is perhaps one of the most crucial aspects of the study of nuclear reactions. Indeed, it is not possible to investigate the properties of a reaction without identifying the fragments produced in charge Z as well as, if possible, in mass A. In addition to this, the identification phase must be performed before the energy calibration.

There are several identification techniques including the $\Delta E - E$ technique and the aforementioned *pulse shape analysis* (PSA) which are primarily used in this work. Specifically, the first method is used for the RCo where the IC-Si and Si-CsI(Tl) correlations can be performed, whereas the second one for the G.A.R.F.I.E.L.D CsI(Tl) crystals.

3.2.1 $\Delta E - E$ technique

This technique uses the energies deposited by a particle in two detectors placed sequentially and it is based on the assumption that the particle stops in the second one. This configuration of detectors is called "telescope". The operating principle of this technique is based on the energy loss mechanism of an ionizing particle passing through an absorber of given density. In the non-relativistic limit, according to the Bethe-Block, formula the energy loss is a function of particle charge Z, mass A and incident energy E [19]:

$$-\left\langle \frac{dE}{dx} \right\rangle \propto \frac{Z^2 A}{E} \tag{3.2}$$

Therefore, the energy loss inside a material is proportional to the square of the impinging particle charge and it increases linearly with the mass of the particle, while it decreases with energy. If one draws the graph of the correlation between the energy lost (ΔE) when crossing the first detector and the energy deposited (E_{res}) in the second, it is observed that when the energy changes the particles are arranged along distinct curves for different values of the product $Z^2 A$ (figure 3.3). Indeed, it can be noted that, at the same atomic number of the incident ion, there is still a separation that depends on its mass. This type of correlation is not normally used for particle identification in G.A.R.F.I.E.L.D. since the PSA method from CsI(Tl) provides more information, in terms of charge and mass, than the $\Delta E - E$ technique. On the other hand, the $\Delta E - E$ method is widely
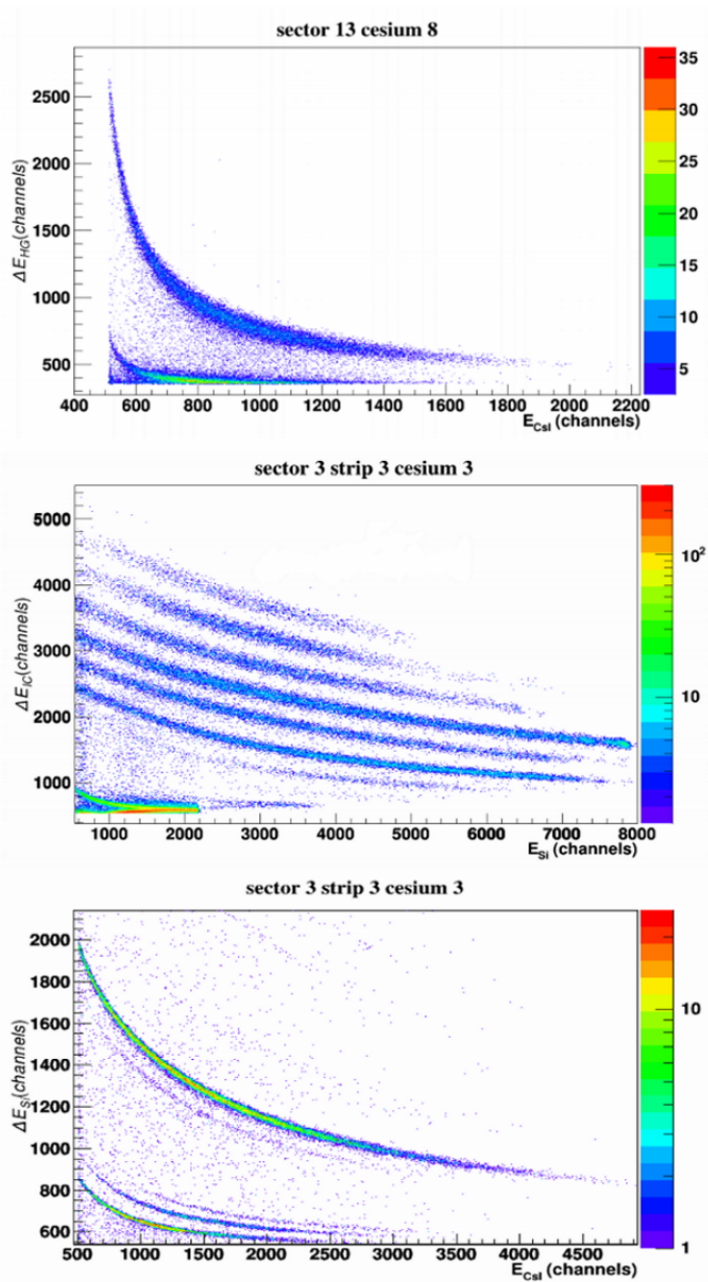
Figure 3.3: The upper panel shows $\Delta E - E$ correlation obtained with a MSGC-CsI(Tl) telescope in G.A.R.F.I.E.L.D. apparatus, whereas in the last two panels there are the $\Delta E - E$ correlations for IC sector 1 and Si strip 2 and for sector 3 Si strip 3 and Cesium 3 in the RCo apparatus [15]. In the second panel it is possible to distinguish Z values up to Z=10. Protons (p), deutrons (d), tritons (t), ^{3}He and α particles can be seen in the lower panel [15].

used for particle identification in the RCo. In this case, two different correlations can be performed. The first one is obtained using a IC-Si telescope, whereas the second one can be built from the ΔE extracted from the Si and the energy from the CsI(Tl). With the last kind of correlation it is also possible to identify isotopes of the detected particle. It should be noted that the only particles that can reach the CsI(Tl) through the first two stages of detection in the studied reaction are the light particles. Examples of $\Delta E - E$ correlation for the RCo are shown in figure 3.3.

3.2.2   Fast-slow PSA in CsI(Tl)

The $\Delta E - E$ identification technique cannot always be applied, for example if the ion stops in the first telescope stage. However, Si and CsI(Tl) detectors enable particle identification through an analysis of the shape of the signal induced by the particle in the detector. As mentioned in section 2.1.2, the CsI(Tl) scintillators emit light pulses whose shape varies as a function of the type of the incident radiation, i.e. it depends on the energy as well as on the charge Z and mass A of the particles. Another important feature of this kind of detector is that its emission spectrum is given by the sum of two exponential terms, one with a short decay time ($\tau_s \sim 0.75 \ \mu s$) and the other with a long decay time ($\tau_l \sim 5 \ \mu s$). Both the value of the two time constants and the distribution of the total intensity between the two components depend on the Z and A of the ion as well as on its energy. In particular, with the same total light emitted, the intensities of the fast and slow components depend on the Z and A of the absorbed ion. Therefore, the *fast* and *slow* components of the CsI(Tl) signals provide a correlation for the particle identification in both G.A.R.F.I.E.L.D and RCo. The two components are extracted by the DSP by applying two filters with the two different constants to the pre-amplified CsI(Tl) signals. The following image shows a reproduction of the light response of a scintillator as a function of the time with the slow component separated from the fast one.
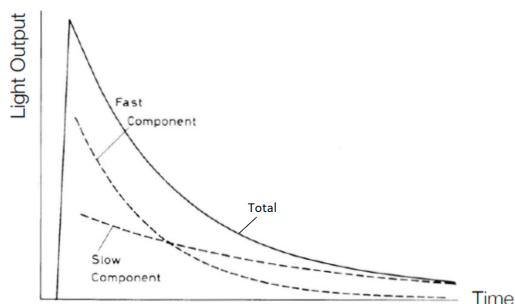

Figure 3.4: Light response of a scintillator as a function of time. The slow and fast components of the light response were separated to show the respective contribution to the total response.

However, a better isotopic separation is gained with the use of a new parameter obtained from a linear mixing of the two components, instead of the direct correlation between fast and slow components. Therefore, the actual correlation performed is the one between the fast component and the *SlowPSA* (spsa) given by:

$$SlowPSA = 3.5 \cdot (long - 4fast) \tag{3.3}$$

Figure 3.5 represents a typical *"Fast vs SlowPSA"* correlation matrix for a chosen G.A.R.F.I.E.L.D. and RCo CsI(Tl) detector in which the three hydrogen isotopes (protons, deuterons and tritons) and the α particles are clearly distinguishable. Finally, the presence of γ-rays characterized by a linear dependence between fast and *spsa* can be noticed. For the scintillators of RCo, due to higher energy particles, also Z=2 isotopes and Z=3 ridges are present.
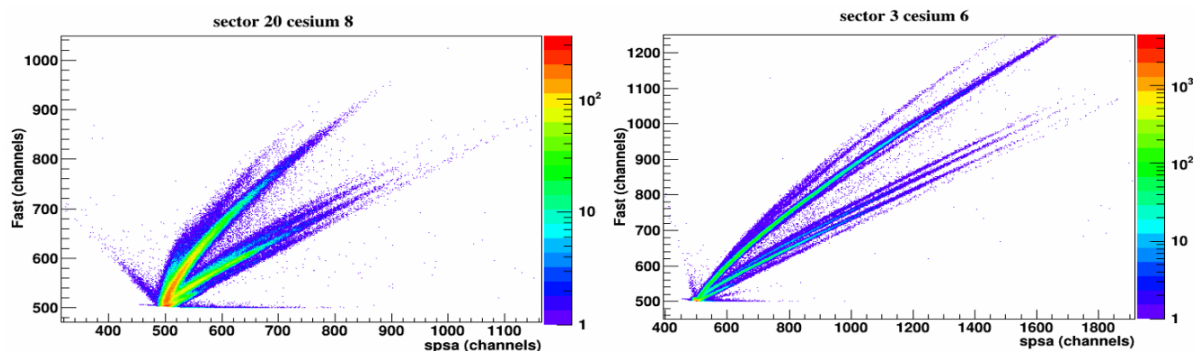
Figure 3.5: *"Fast and spsa"* correlation for the Cesium 8 sector 20 of G.A.R.F.I.E.L.D. (left panel). From the bottom one can recognize the ridges corresponding to γ, p, d, t and α particles, respectively. The same correlation is shown for the Cesium 6 sector 3 of RCo (lright panel) [15]. Here, above the ridge corresponding to tritons, ^{3}He, α and Li ridges are clearly visible.

3.3 Data structure and observables

For the data analysis the ROOT code [20] has been used. A *TTree* is a ROOT data structure used for storing, reading and analysing a large number of entities consisting of a heterogeneous set of data of various types. It is an object belonging to the *TTRoot class* optimized to reduce disk space and speed access in I/O and it features a great flexibility in the analysis phase. A TTree can handle any type of data that is organized hierarchically in memory addresses like *TBranches*, each of which can contain substructures called *Tleaf*. Each of these "leaves" represents the memory address where a single data is saved.

In the present thesis, all the experimental data are collected in an n-tuple which is a special kind of TTree. Specifically, a n-tuple is an array characterized by *float* type variables for each column and whose rows represent events. An event is defined as what is collected by the acquisition system in the time interval between a trigger signal and the next one. The total number of events corresponds to the number of the acquisitions made during the measurement shifts. Once acquired, the events are saved in the n-tuple. Within each event many variables, that have a multiplicity that represent different signals produced in the same event, are included. For this reason, *event variables* are distinguished from those of *multiplicity*. Both types are of fundamental importance for the analysis. Indeed, within the data analysis program they provide the possibility to make selections aimed at sorting the physical events of interest. This is possible through the so-called *event* or *multiplicity cycles*, which are iterated only if the conditional expressions of control on the event or multiplicity variables are satisfied. It is important to highlight that before using all the variables of interest within the program, it is necessary to read the various memory addresses in which all the data in the n-tuple are saved. In this analysis phase, the TBranches can be read selectively by the program in order to obtain an optimized data reading performance [20].

Among the event variables the most important and most used are:

- *ztotrco* and *ztotgf*: these variables represent, respectively, the total sum of all the charges detected in the Ring Counter and in G.A.R.F.I.E.L.D., respectively.

- *mult*: it indicates the number of products or fragments in a single event. It is, in general, the variable used for the multiplicity cycles.

- *ma*: this variable stands for the number of α-particles in the single event.

- *ncrco*: it represents the multiplicity of charged particles that are detected in the RCo.

- *mgarf*: this variable is similar to the previous one since it stands for the multiplicity of detected charged particles in G.A.R.F.I.E.L.D.

Some examples of multiplicity variables widely used in this analysis are:

- *numtel*: it indicates the identification number of the detector associated with the particle detection. It includes two "chambers" of detection. If this variable has a value between 1 and 248, it indicates that the particle has been detected in one of the G.A.R.F.I.E.L.D. telescopes. In this case, the last digit of this number, which can be between 1 and 8, represents the Cesium detecting the particle. The remaining digits have a number between 1 and 24 and indicate the sector in which the particle is located. On the other hand, values above 3000 have been chosen to indicate that the particle has been detected in the RCo. The notation is similar to the previous case with the exception that the digit 3 is added before the number. The second digit stands for the sector, the third for the Si strip and the fourth for the CsI(Tl) (this value could be zero if the particle stops in the Si detector).

- z and a: these are both multiplicity variables which represent the charge Z and the mass number A of the detected particle.

- *ei*: this variable represents the energy of the incident particle. Within the program it is used to calculate the sum of the energies of the α-particles in the events involving four α-particles. This quantity is necessary to calculate the excitation energy of the target and then of the projectile as will be described in the next paragraphs.

- *vx*, *vy* and *vz*: they are the three velocity components of the detected particle used to derive the momentum components of each particle necessary to obtain the total momentum and the recoil momentum. The latter allows to obtain the target recoil energy, a quantity that will be used to calculate the excitation energy of the target.

3.4 Data selection

As explained in section 2.3.1, a preliminary selection of particular physical conditions was made already in the data acquisition phase by using combinations of trigger signals. This allows to acquire only the events that, at first, are of interest and to neglect those which are not. Subsequently, during the analysis phase, other selections have been performed, aimed at isolating the events of interest among all the detected ones.

3.4.1 Selection of events of interest

Since the purpose of this thesis is the study of the decay of the excited ^{16}O nucleus, either through the ^{12}C $+ \alpha$ or two ^{8}Be, into a final state consisting of four α-particles, it is necessary to make a selection of events in which four α-particles are present in the final state of the system. In particular, since the α particles are emitted by the QP which travels in the forward direction, only the reactions in which these alpha particles are emitted at forward angles are selected. This means that the α particles are only detected in the RCo. In addition this selections allows for QT not detected because of its energy lower than the detector thresholds.

In this case, two different type of analyses can be performed. The first one uses both charge and mass identification.

It was possible to do this by imposing a condition on some of the variables listed in the section 3.3. Specifically, it was imposed that the multiplicity of the detected α-particles *ma* and the multiplicity of particles detected by the RCo *ncrco* assumed the value 4. In addition to this, the possibility of detecting some particles inside G.A.R.F.I.E.L.D. is excluded by assuming that the multiplicity of particles detected by the G.A.R.F.I.E.L.D. apparatus *mgarf* must be equal to 0.

In this experiment, two different type of analyses can be performed: the first one uses both charge and mass identification of the detected α-particles, by imposing the condition of having Z=2 and A=4 for each of the detected particle. The other one, which is the one carried out in this thesis, considers only the Z=2 condition. In this way, also the α particles whose mass could not be identified are also included in the selection. Therefore, this type of analysis includes the first one. As said in section 3.2, the most used identification method was the $\Delta E - E$ technique. Indeed, the mass identification for α particle is possible only for the ones which punch through the silicon detector, implying that the threshold for mass identification is of the order of 24 MeV.

3.4.2 Energy balance of the decay

Starting from the energy of the reaction products it is possible to recreate the decay dynamics from an energetic point of view. Indeed, the projectile and target excitation

energies can be obtained from the energy of the particles produced during the reaction, which, in this case, are α particles.

It is well known that in every physical reaction the principle of energy conservation must be valid. Therefore the total energy of the system will be given by the following expression:

$$E_{tot_i} = E_{beam} = E_{tot_f} = \sum^{4} E_{\alpha} + E_{target} - Q \tag{3.4}$$

where E_{tot_i} and E_{tot_f} stand for the initial and final total energy, respectively. Q is known as *Q-value* and indicates the difference between the rest masses of the reagents and products of the reaction. Finally, E_{beam} is the the energy of the incident oxygen beam, whereas E_{target} is the total energy of the QT, given by:

$$E_{target} = E_{rec} + E_{exc_t} \tag{3.5}$$

E_{exc_t} and E_{rec} represent the QT excitation energy and recoil energy. The latter is obtained by the conservation of the impulse in the laboratory system starting from the momentum of the four α particles. The principle of impulse conservation implies that the QP impulse, after the impact ($\vec{P}_{beam_f}$), must be equal to the sum of the impulses of the detected four α particles:

$$\vec{P}_{beam_f} = \sum^{3} \vec{P}_{\alpha} \tag{3.6}$$

Since the impulse of the initial beam is known, it is possible to obtain the recoil impulse $\vec{P}_{rec}$ of the target and finally obtain the recoil energy E_{rec} of the latter after the impact. Indeed,from the dynamics of the reaction one has:

$$\vec{P}_{beam} = \vec{P}_{beam_i} = \vec{P}_{beam_f} + \vec{P}_{rec} \tag{3.7}$$

with

$$|\vec{P}_{beam}| = P_{beam_z} \tag{3.8}$$

It should be noted that $P_{beam_z}{}^2$ can assume different values based on the energy of the incident beam, specifically 1975, 1638 and 1811 MeV/c for an incident energy of 130, 110 and 90 MeV.
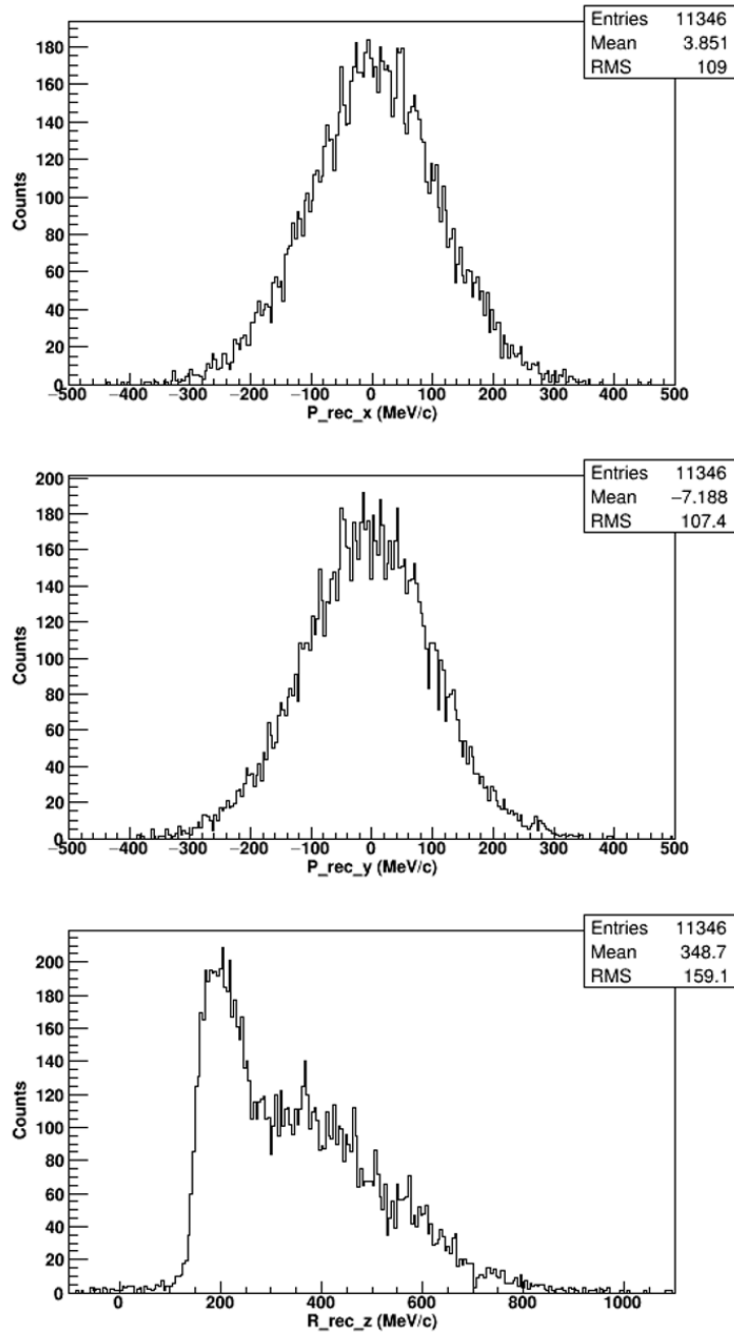
The three components P_{rec_x}, P_{rec_y} and P_{rec_z} of the recoil pulse are shown in figure 3.6 and are calculated through the following expressions derived from the impact dynamics:

$$P_{rec_z} = P_{beam_z} - \sum^{4} P_{\alpha_z} \tag{3.9}$$

$$P_{rec_y} = -\sum^{4} P_{\alpha_y} \qquad P_{rec_x} = -\sum^{4} P_{\alpha_x} \tag{3.10}$$

---

[2]z has been assumed for the beam direction.

Figure 3.6: X, Y and Z components of the recoil impulse of the QT after the impact. The first two distributions are centered around 0 value because the initial trasverse impulse is zero.

Once the recoil impulse has been calculated, it is possible to obtain the recoil energy of the QT, after the impact, by means of the following formula:
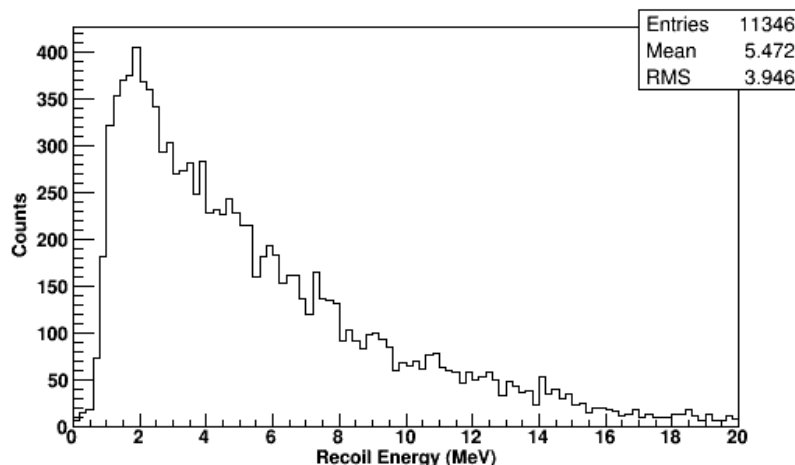
$$E_{rec} = \frac{|\vec{P}_{rec}|^2}{2M} \tag{3.11}$$

Figure 3.7: Recoil energy of the target after the impact.

It is assumed that the mass M, which appears in the equation 3.11, has the value 11178 MeV/c^2, since the QT is considered as a nucleus with A=12.

3.5 Target excitation

As described in section 1.2, in a peripheral collision, following the interaction between the projectile and the target, a QT is produced in its ground state or in one of its excited states. Since in the data selection we have considered only events with no particles in the G.A.R.F.I.E.L.D. detector, the QT can be excited below the threshold for particle emission. The energy spectrum of the QT can be derived by applying the formulas in section 3.4.2. Indeed, by replacing the equation 3.5 in 3.4 and by reversing the expression, the resulting formula is:

$$E_{exc_t} = E_{beam} - E_{rec} - \sum^4 E_\alpha + Q \tag{3.12}$$

where Q is the ^{16}O $\to$ 4α breakup threshold energy, which is 14.433 MeV.

Considering the $\sum^4 E_\alpha + E_{rec}$ quantity, this turns out to differ from the QT total energy due to the QT excitation energy and the Q-value. Therefore, for each event the

energy $\sum^4 E_\alpha + E_{rec}$ corresponds to a specific value of the QT excitation energy. By representing the quantity in a graph, it is possible to obtain the energy spectrum of the QT in which the corresponding peaks to the ground and excited states of the QT nucleus can be observed (figure 3.8). In particular, the ground state appears together with the first γ excited state at 4.4 MeV. The queue to lower energies is due to particles coming from the decay $^{12}C^*$ highly excited with decay products not completely detected due to the apparatus efficiency.
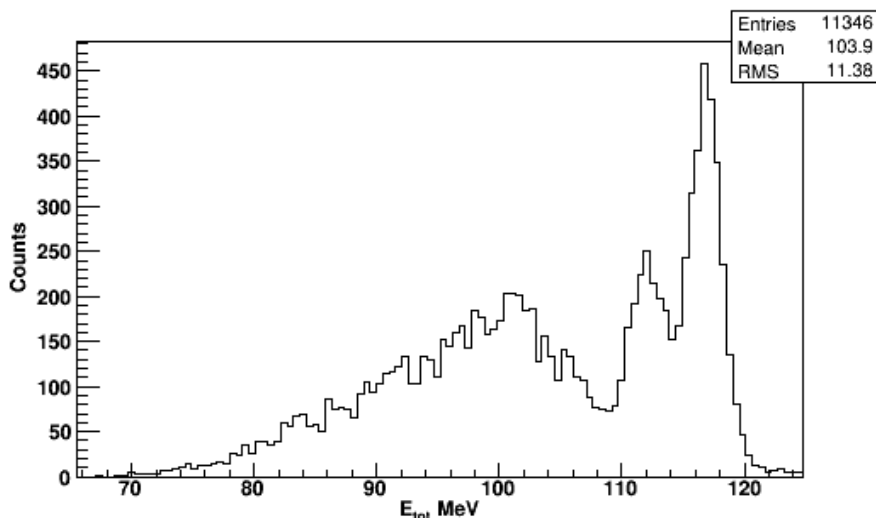
Figure 3.8: Total energy of the four produced α particles added to the QT recoil energy.

Once the energetic spectrum of QT has been obtained, three different types of analysis can be carried out. The first type selects only the events which fall within the first peak to the right, that indicates the ground state of the QT. Therefore, this analysis only considers the events in which the QT remains in its ground state. On the other hand, the second one selects the events which fall within the second peak. These are all the events in which the QT is excited to its 4.4 MeV excitation energy state. Finally, the third analysis includes the first two analyses by selecting both aforesaid peaks, in order to obtain a larger statistics. All the selections performed are shown, in the order in which they are carried out, in figure 3.9.
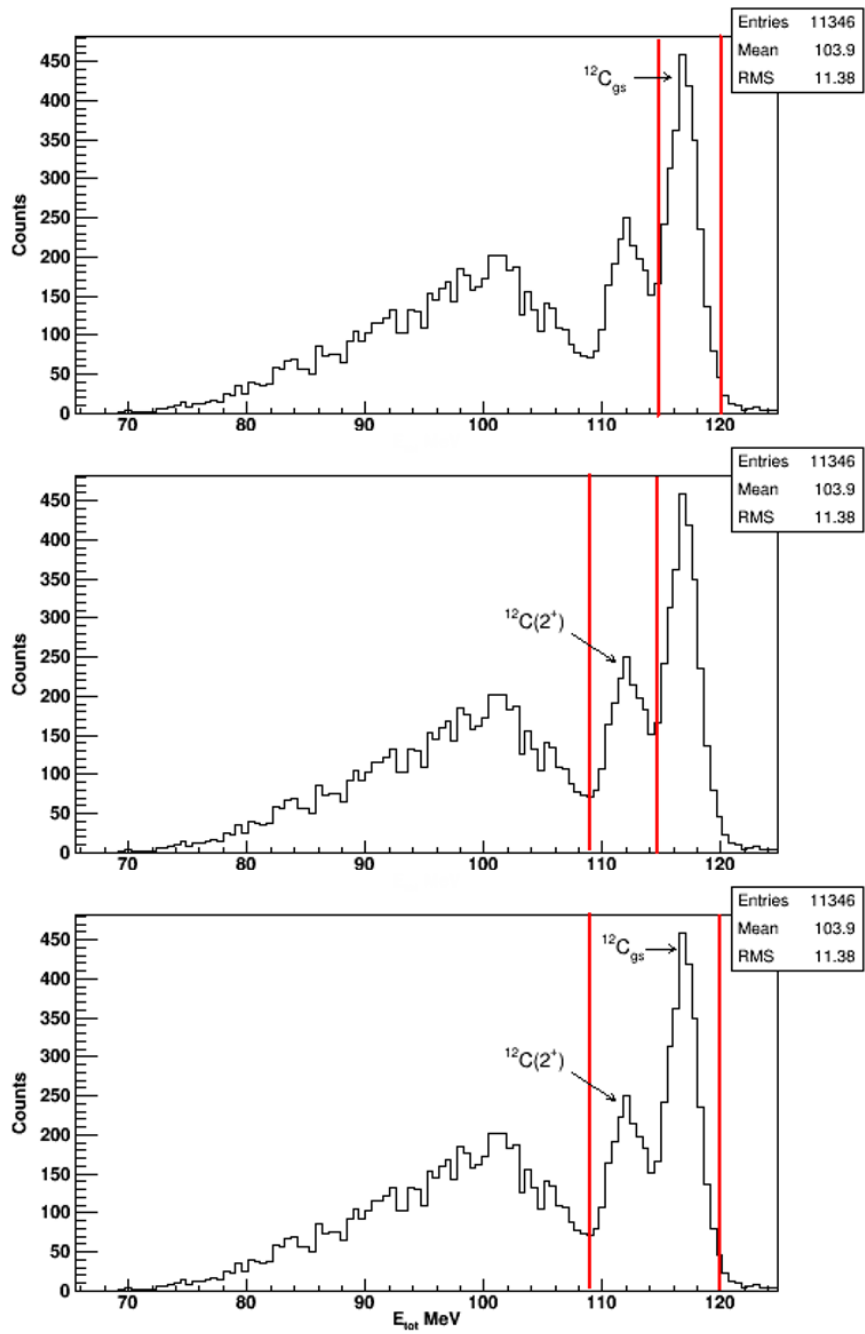
Figure 3.9: Selections of the events in the three analyses performed.

3.6   Projectile excitation

Within the selections made in the experimental data, the excitation energy of ^{16}O ($E_x(^{16}$O)) can be reconstructed from the momenta of the four α particles, through the relationship

$$E_x(^{16}O) = Q + \sum_{i=1}^{4} E_i(\alpha) - E(^{16}O) \tag{3.13}$$

where

$$E(^{16}O) = \frac{[(\sum_{i=1}^{4} P_{\alpha_i}(x))^2 + (\sum_{i=1}^{4} P_{\alpha_i}(y))^2 + (\sum_{i=1}^{4} P_{\alpha_i}(z))^2]}{2M(^{16}O)} \tag{3.14}$$

Q is equal to 14.433 MeV and corresponds to the Q-value already mentioned in section 3.5, whereas $P_{\alpha_i}(x)$, $P_{\alpha_i}(y)$ and $P_{\alpha_i}(z)$ are the x, y and z momentum components of the α particles. In this case, as specified in the equation, M is the mass of QP with a value of 14904 MeV since the QP is a nucleus with A=16. The equations 3.13 and 3.14 produce an ^{16}O excitation energy spectrum, i.e. of the QP before it decays, which is independent of the details of the successive emission of the four α particles. Figure 3.10 shows the ^{16}O excitation energy spectrum for all 4α-particles events in which the ^{12}C recoil was in the ground state.
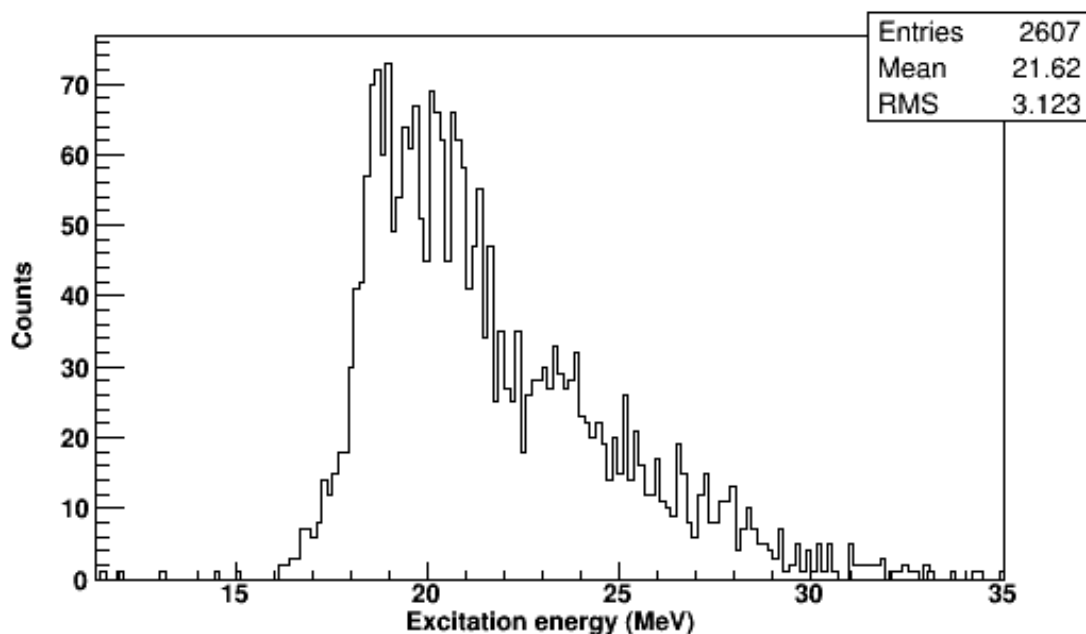

Figure 3.10: Excitation energy of ^{16}O QP after the impact.

The detection of the four α particles enables a reconstruction of the decay process

of the ^{16}O excited state. As already explained in section 1.3.1, the main decay channels that may be observed in this experiment are:

- the symmetric decay of the QP nucleus into two ^{8}Be nuclei, each of which, in turn, decays into two α particles, thus resulting in four α particles in the final state of the system;

- α decay to the ^{12}C($7.65\ MeV, 0_2^+$) excited state, which then decays to ^{8}Be + α; the final state of 4 α-particles is due to the decay of ^{8}Be in 2 α-particles.

- α decay to the ^{12}C($9.64\ MeV, 3^-$) excited state, which also decays to ^{8}Be + α, and finally in 4 α-particles like the previous channel.

In order to determine if the QP decays through the two ^{8}Be nuclei channel, the excitation energies in two ^{8}Be were obtained starting from all possible combinations of a couple of α particles out of the four. For this purpose, the relative energy among the α particles of each pair is calculated. Then the relative energy of the couple providing the lowest value is sorted out and represented in the graph shown in figure 3.11. This energy is then evaluated in order to find out if it falls within the peak at 92 keV above the ^{8}Be $\rightarrow$ 2α decay threshold, representing the ground state of the ^{8}Be nucleus [9]. A selection of data
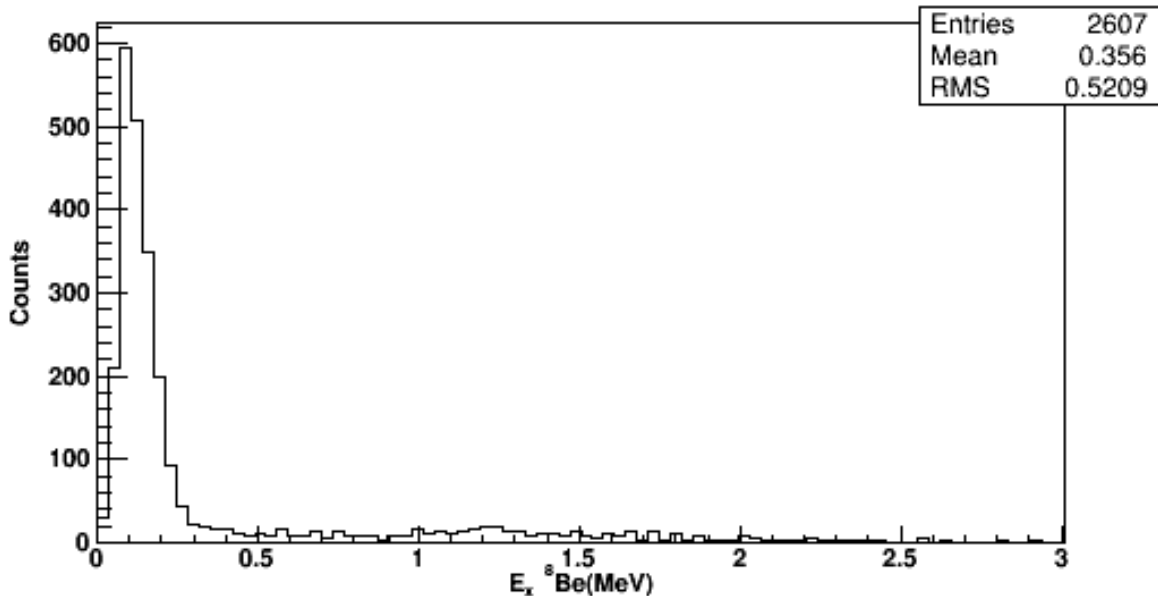
Figure 3.11: Relative energy between two α particles in the couples providing the lowest value.

falling within the range $0 \div 0.3\ MeV$, i.e. of those that are included in this peak, is

made. By means of this kind of selection, all events, in which at least one ^{8}Be nucleus in its ground state is formed, are found. Being focussed on two ^{8}Be nuclei channel, the study requires a further selection for the couples that are complementary to those that have provided the lowest relative energy value. Therefore, the relative energy of these couples is represented in a graph and a further selection of data is carried out (figure 3.12). Also in this case, the relative energy of the complementary couples is checked to determine if it falls within the peak at 92 keV. For this reason, a selection of data within
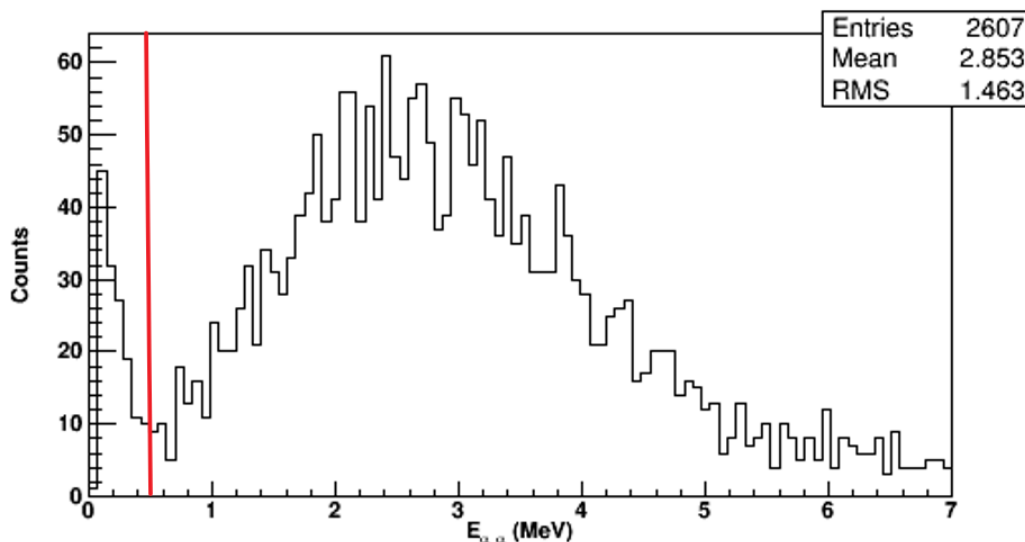
Figure 3.12: Relative energy between two α particles in the couples complementary to those which provide the lowest value. The red line represents the dividing line of the selection made.

the range $0 \div 0.5 \; MeV$ is performed. Hence, also considering the previous selection, only the events in which two ^{8}Be nuclei are formed are taken into account.

In a similar way, in order to determine if the four α particles detected are originated from a ^{12}C nucleus with excitation energy of 7.65 and 9.64 MeV, all the possible sets of three α particles out of the four are considered.

As a first approximation, the events are selected where two α particles come from a ^{8}Be nucleus coming from the same data selection made for the previous decay channel, i.e. considering only the values of the minimum relative energy provided by α couples which fall within the range $0 \div 0.3 \; MeV$. In addition we have considered that the complementary couples assume a relative energy value higher than 0.5 MeV (figure 3.12), a range complementary to the one selected in the case of the two ^{8}Be nuclei channel $(0 \div 0.5 \; MeV)$.

Once these selections are carried out, from the excitation energy of each α particle triple, the excitation energy of carbon is calculated as the minimum energy of these

four triples. This amount is added to the energy of the fourth α particle, which does not belong to the triple, to obtain the excitation energy of the ^{16}O QP. The results are shown in figure 3.13.
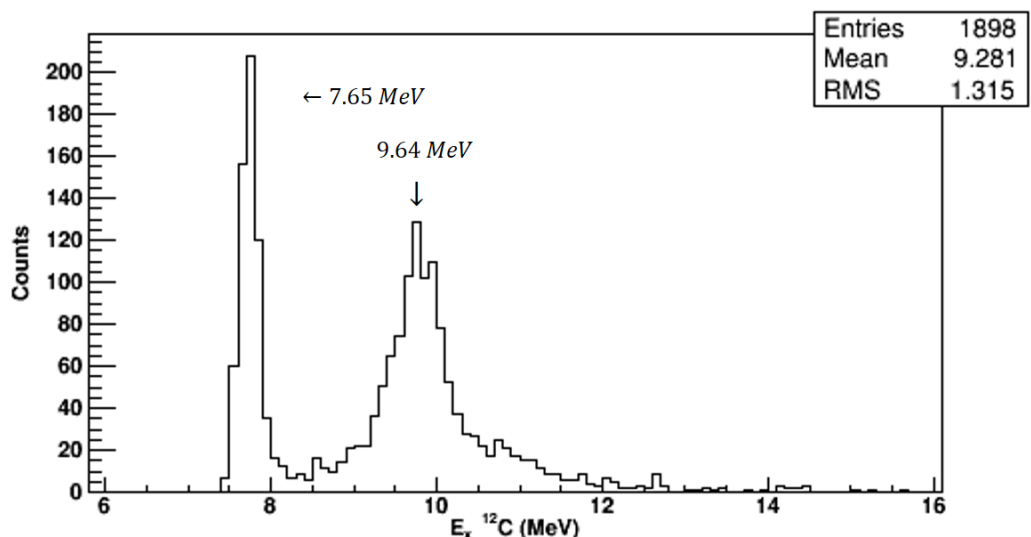

Figure 3.13: Excitation energy spectrum of carbon in which the excited ^{16}O QP decays with the emission of an α particle.

It should be noted that in this spectrum the two excited carbon states can be distinguished. The selection of the data that fall within the 7.65 or 9.64 MeV peak enables to study, separately, the two decay channels in which an excited carbon nucleus is formed. The first peak corresponds to the presence of a ^{12}C nucleus in the Hoyle excited state (7.65 MeV), whereas the second one is associated to a ^{12}C nucleus in a 3^- state at 9.64 MeV excitation energy. Specifically, for the first decay channel the events in which the minimum carbon excitation energy is between 7.4 and 8.2 MeV are selected, while for the other one only the data which fall within 9.0 and 10.6 MeV are considered. Under these conditions, the excitation energy of the projectile is plotted in order to obtain the oxygen excitation spectrum for each decay channel. Finally, in order to obtain a more comprehensive view of the statistics, a quasi-projectile excitation energy spectrum is obtained by taking into account both last decay channels described. This is possible by selecting simultaneously the data that fall within the first and second peak.

3.6.1   QP decay with QT in ground state

The first case taken into account is the one in which the QP decays, whereas the QT takes part of the energy by transforming it into recoil kinetic energy, while remaining in its ground state. As described in section 3.5, this kind of events are those for which

only the first peak in the spectrum of the excitation energy of the QT has been selected (figure 3.9, first panel). The first QP excitation energy spectrum obtained refers to the two ^{8}Be decay channel and it is shown in figure 3.14.
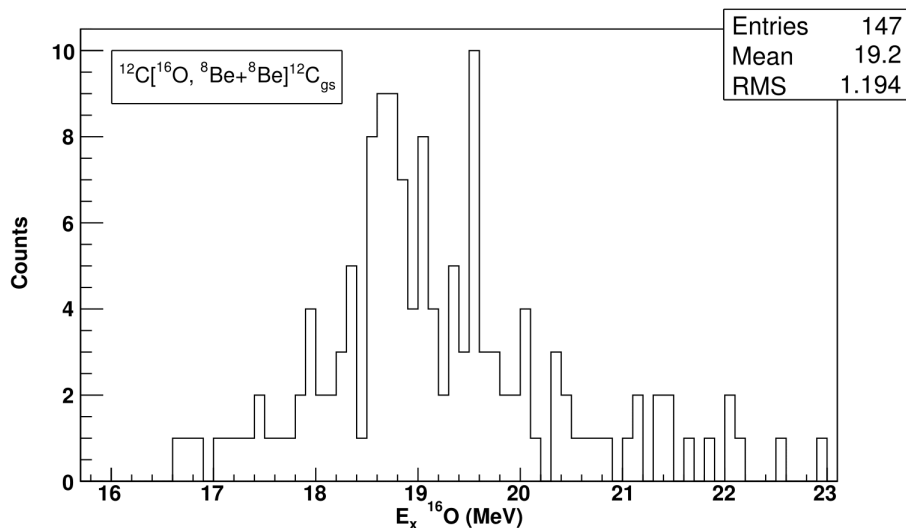
Figure 3.14: ^{16}O excitation spectra for the ^{12}C[^{16}O, ^{8}Be + ^{8}Be]^{12}C$_{gs}$ decay channel.

Given a total number of events of 2607, in which the QT is in its ground state, only 147 of these correspond to a two ^{8}Be nuclei decay channel. Therefore, this decay process accounts for 5.6 % of the occurrences.

$$N_{ev} = \frac{147}{2607} \sim 5.6\% \qquad (3.15)$$

Table (3.1) compares the energy levels that can be distinguished in the spectrum obtained with those listed in the online archive NUDAT2 [21].

The two remaining excitation spectra of the QP are associated to the decay process in which the excited QP, after the impact, decays in two different ^{12}C excited states. Figure 3.15 shows the QP energy spectrum in the case of the ^{12}C in Hoyle excited state (upper panel) and in the 3$^-$ state (lower panel). The first decay process accounts for 24% of the occurrences, since in a total of 2607 events it occurs 614 times:

$$N_{ev} = \frac{614}{2607} \sim 24\% \qquad (3.16)$$

The last decay channel, instead, accounts for 37% of the occurrences, since:

$$N_{ev} = \frac{958}{2607} \sim 37\% \qquad (3.17)$$

NUDAT2 levels (MeV)	$J^{(p)}$	Width (keV)	Observed levels (MeV)
18.016	4^+	14	17.9
18.404	5^-	550	18.3
18.600	$1^-, 5^-$	150	18.7
19.08	2^+	120	19.1
19.375	4^+	23	19.3
19.539	2^+	255	19.5
20.005	2^+	400	20

Table 3.1: Comparison between some levels listed in the online archive NUDAT2 corresponding to the ones obtained in this experiment for the $^{12}\text{C}[^{16}\text{O}, \,^8\text{Be} + \,^8\text{Be}]^{12}\text{C}_{gs}$ decay channel.
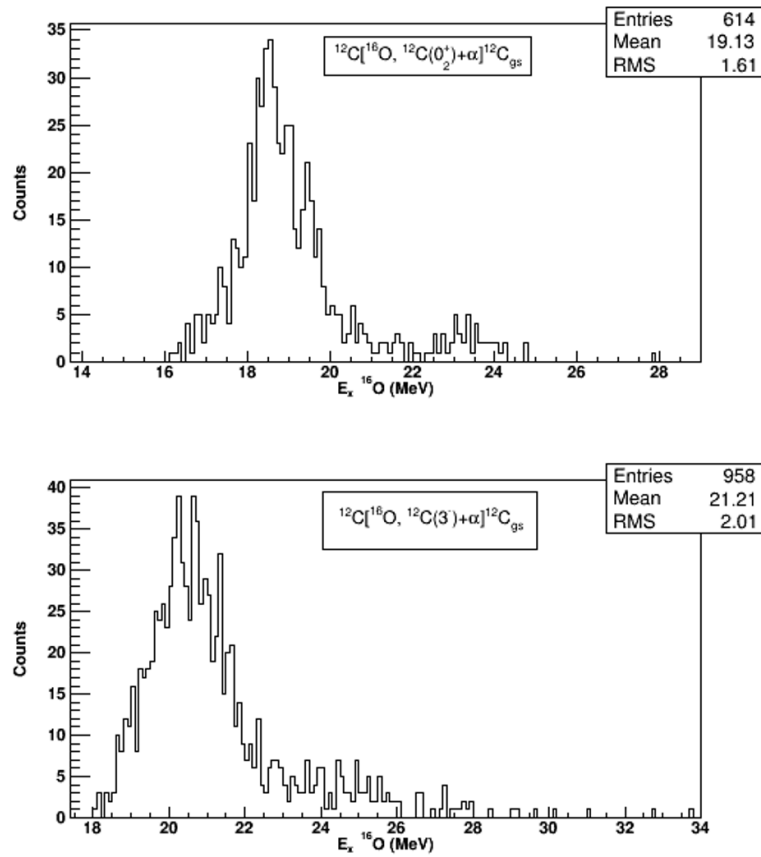
Figure 3.15: a) Excitation energy spectrum of the QP in the $^{12}\text{C}[^{16}\text{O}, \,^{12}\text{C}(0_2^+) + \alpha]^{12}\text{C}_{gs}$ decay channel. b) Excitation energy spectrum of the QP in the $^{12}\text{C}[^{16}\text{O}, \,^{12}\text{C}(3^-) + \alpha]^{12}\text{C}_{gs}$ decay channel.

Two tables (3.2 and 3.3) are included for these decay channels to compare the observed energy levels with those mentioned in the literature.

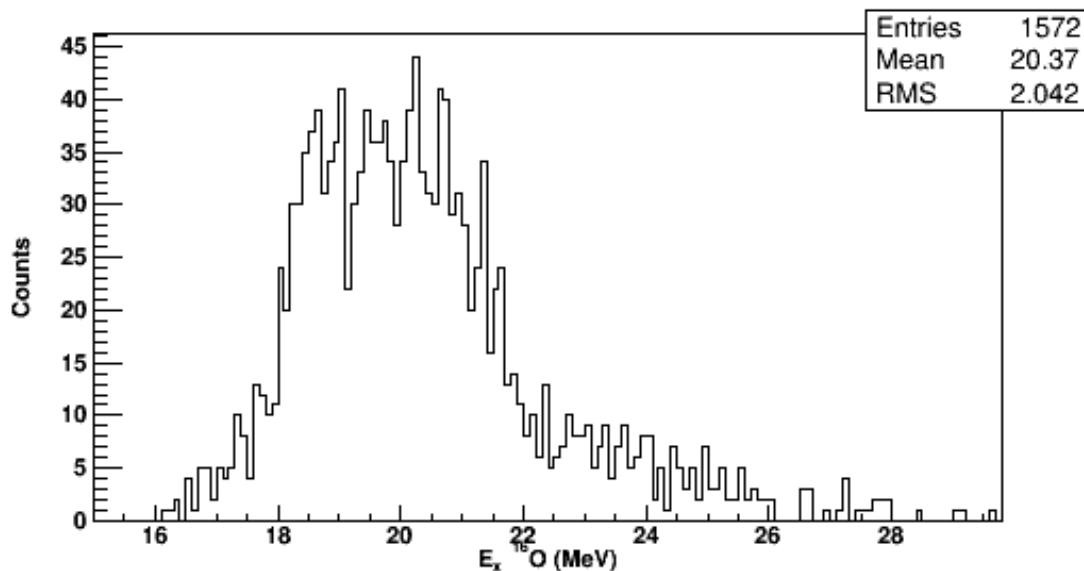| NUDAT2 levels (MeV)	$J^{(p)}$	Width (keV)	Observed levels (MeV)
17.282	1^-	78	17.4
17.609	2^+	114	17.7
18.089	0^+	288	18
18.290	3^-	380	18.2
18.600	$1-,\ 5-$	150	18.6
19.080	2^+	120	18.9
19.539	2^+	255	19.4
19.754	2^+	400	19.7

Table 3.2: Comparison between levels listed in the online archive NUDAT2 and those obtained in this experiment for the $^{12}\text{C}[^{16}\text{O},\ ^{12}\text{C}(0_2^+) + \alpha]^{12}\text{C}_{gs}$ decay channel.

NUDAT2 levels (MeV)	$J^{(p)}$	Width (keV)	Observed levels (MeV)
19.080	2^+	120	18.9
19.754	2^+	290	19.7
20.615			20.6
21.052	6^+	205	20.9
22.350	2^+	175	22.3

Table 3.3: Comparison between levels listed in the online archive NUDAT2 and those obtained in this experiment for the $^{12}\text{C}[^{16}\text{O},\ ^{12}\text{C}(3^-) + \alpha]^{12}\text{C}_{gs}$ decay channel.

Finally, by selecting the data that fall inside the one or the other peak in figure 3.13, one can obtain the energy spectrum of the the ^{16}O QP for both decay channels that feature an excited ^{12}C as the one shown in figure 3.16. Once again, here follows a table (tab. 3.4) comparing the various energy levels observed.

It is important to highlight that, in the last two spectra (figures 3.15 panel b) and 3.16) some peaks have emerged at energies that do not correspond to any known energy level. This could be due to the resolution or to the physical limitation of the apparatus, which can shift the position of known levels, or to new levels not known from previous measurements.
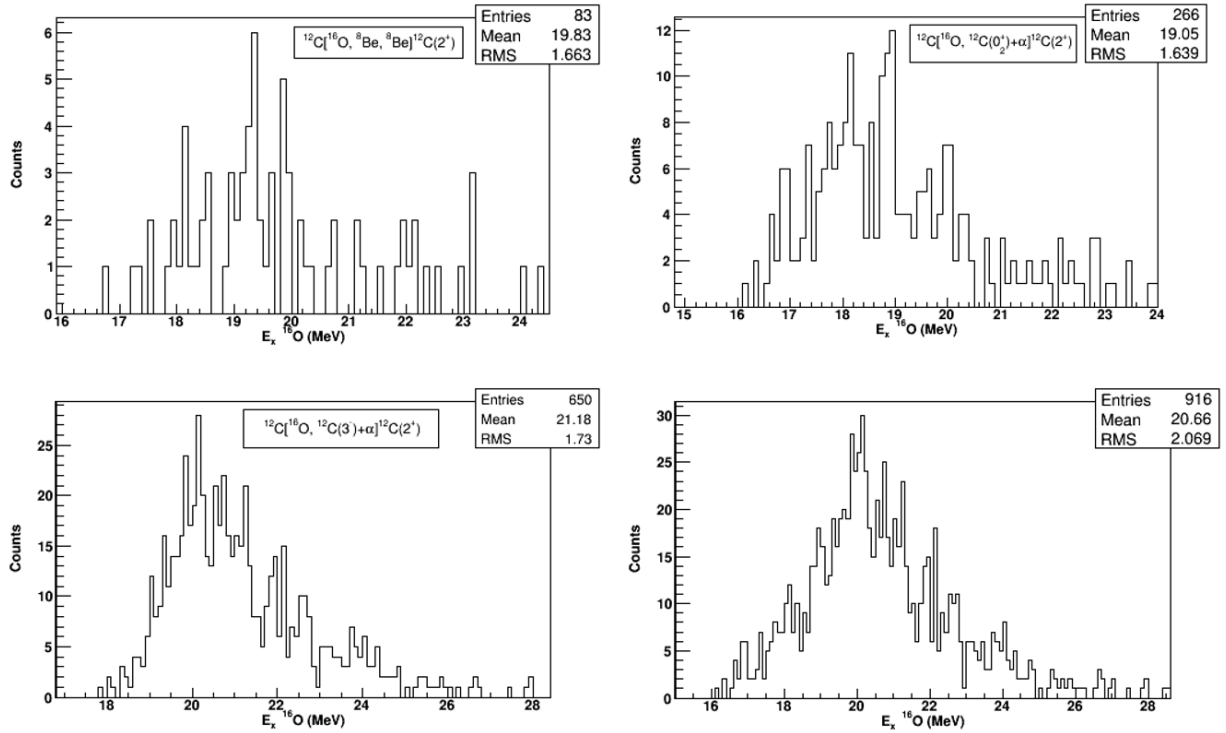
Figure 3.16: ^{16}O excitation spectra for both ^{16}O$^* \to 12$C$^* + \alpha$ decay channels.

NUDAT2 levels (MeV)	$J^{(p)}$	Width (keV)	Observed levels (MeV)
17.282	1^-	78	17.4
17.609	2^+	114	17.6
18.600	$1-, 5-$	150	18.6
19.080	2^+	120	19
19.539	2^+	255	19.4
19.754	2^+	290	19.7
21.623	7^-	60	21.6
22.350	2^+	175	22.3

Table 3.4: Comparison between levels listed in the online archive NUDAT2 and those obtained in this experiment for the ^{16}O$^* \to \, ^{12}$C$^* + \alpha$ decay channels.

3.6.2   QP decay with QT in excited state

The next case examined features the QP decay while the QT takes energy from the projectile which therefore reaches the first excited state (^{12}C$(2)^+$). The analysis carried out for this second case is similar to the one performed for the previous one (section 3.6.1). The only difference is that the data included within the second peak of the excitation energy spectrum of the QT (second panel of figure 3.9) are selected. By applying the considerations made above, the energetic spectra of the excited QP for the three decay channels studied and, finally, for both α decay channels in ^{12}C* can be obtained.

49

Figure 3.17: ^{16}O excitation spectra for ^{12}C[^{16}O, ^{8}Be + ^{8}Be]^{12}C(2)$^+$ and ^{12}C[^{16}O, ^{12}C(0$_2^+$) + α]^{12}C(2)$^+$ decay channels are shown in the upper left and right panel, respectively. The spectra for ^{12}C[^{16}O, ^{12}C(3$^-$) + α]^{12}C(2)$^+$ and ^{16}O* $\rightarrow$ ^{12}C* + α decay channels are shown in the lower left and right panel, respectively.

3.6.3 QP decay with QT in ground or excited state

The last case dealt with the inclusion of all the events where the formation of an excited QP takes place and where the QT produced can be in its fundamental state or in one of its excited state. To select this type of events it is sufficient to consider only the data that fall within one or the other peak of the excitation energy spectrum of the QT, as shown in the third panel of figure 3.9. Basically, this type of analysis is a combination of the two previously described. The energy spectra of the excited QP obtained in this way, for the various decay channels, are shown in the following figures. This last analysis can be a useful tool to provide a broader statistic of the type of reactions studied.
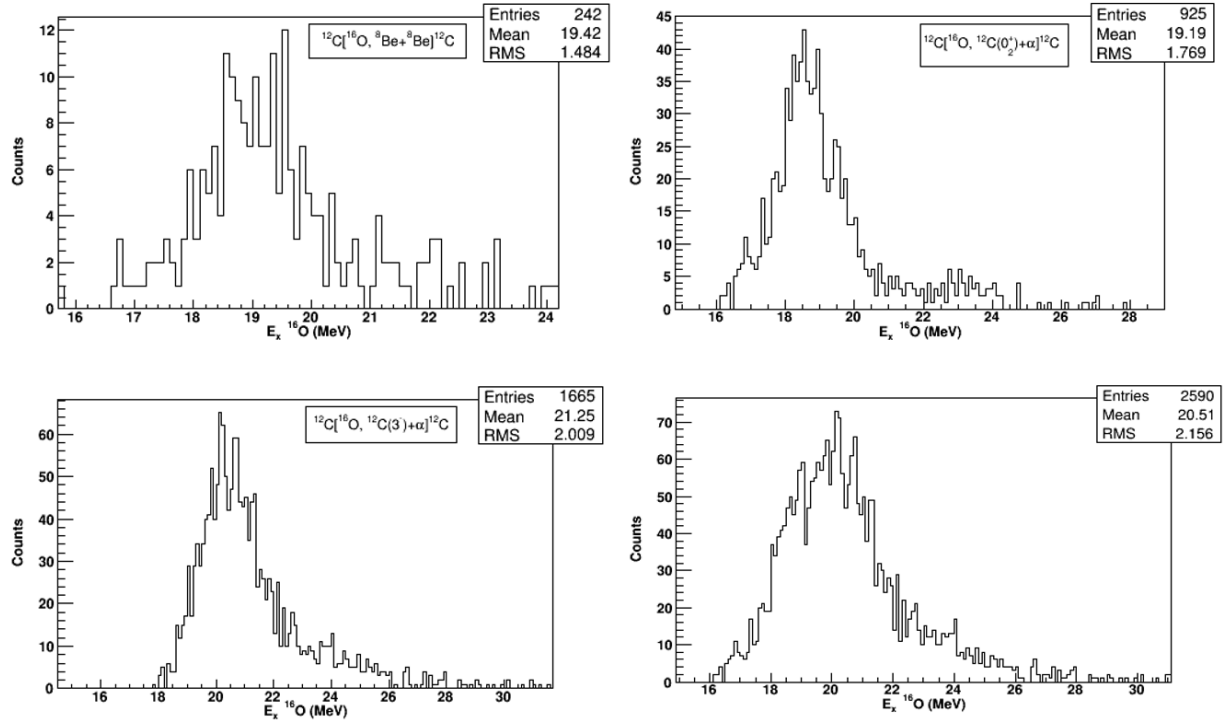
Figure 3.18: ^{16}O excitation spectra for ^{12}C[^{16}O, ^{8}Be + ^{8}Be]^{12}C and ^{12}C[^{16}O, ^{12}C(0_2^+)+α]^{12}C decay channels are shown in the upper left and right panel, respectively. The spectra for ^{12}C[^{16}O, ^{12}C(3^-) + α]^{12}C and ^{16}O* $\rightarrow$ ^{12}C* + α decay channels are shown in the lower left and right panel, respectively.

Conclusions and perspectives

The analysis of the $^{16}O^*$ decay in four α-particles, with excitation energy in the interval between 17 and 22 MeV has been performed. A predominance of a sequential decay proceeding through the evaporation of an α-particle with the consequent formation of a $^{12}C^*$ has been found. The $^{12}C^*$ in turn evaporates an α-particle and the residue is a $^8Be_{gs}$. Finally, the $^8Be_{gs}$ decays in two α-particles. The channel not going through the $^{12}C^*$ consists in a decay in two $^8Be_{gs}$, which both decay in turn in two α-particles. The probability of this channel is of the order of 5%. The second results of this analysis consists in the identification of several levels in the reconstructed $^{16}O^*$ excitation spectrum. Some of the levels listed in the nuclear database NUDAT2 are present in the data. The levels contributing to the decay channels are different one from the other. Some peaks do not correspond to known levels. This can be due to experimental resolution or indetermination, to interference between levels or even to levels not yet experimentally found. Further analysis are needed to explain these discrepancies. In particular, it will be performed a Monte Carlo calculation with codes based on the statistical decay of light nuclei. Indeed, a specific decay code has been developed, within the NUCL-EX collaboration, which is based on the Hauser-Feshbach formalism, and takes into account all the known levels of light ions. Agreement or disagreement with statistical decay code could indicate the relative importance of clustering effects, i.e. effects related to the structure of even nuclei based on α-particles to be compared to single particle structure such as the one described by the shell model.

Bibliography

[1] D. Durand, E. Suraud and B. Tamain, **Nuclear Dynamics in the Nucleonic Regime**, ed. IoP, London, 2001. ed. John Wiley and Sons, 1988.

[2] K.S. Krane, **Introductory nuclear physics**, ed. John Wiley and Sons, 1988.

[3] M. Freer, **Rep. Prog. Phys. 70 2149**, 2007.

[4] W.Catford, **Clustering in Nuclei from N/Z=1 to N/Z=2**, arXiv:1302.3849, 2013.

[5] K. Ikeda *et. al.*, **Prog. Theor. Phys. 68, 1980**, 1979.

[6] W. von Oertzen, **Eur. Phys. J A 11, 403**, 2001.

[7] P. Chevallier *et al.*, **Phys. Rev. 160, 827**, 1967.

[8] N. Curtis *et. al.*, **Phys. Rev. C 88, 0643309**, 2013.

[9] M. Freer *et. al.*, **Phys. Rev. C 51, 1682**, 1995.

[10] M. Bruno *et. al.*, **Eur. Phys. J.A 49, 128**, 2013.

[11] S. Carboni *et. al.*, **Nucl. Instr. and Meth. A, 664, 251-263**, 2012.

[12] FAZIA Collaboration: http://fazia.in2p3.fr/?lang=en

[13] N. Le Neindre *et. al.*, **Nucl. Instr. and Meth. A 701, 145**, 2013.

[14] L. Bardelli, **A ROOT-based data-monitor software for the GARFIELD experiment, LNL Ann. Report**, 2007.

[15] C. Frosin, **Master Thesis: The ^{16}O + ^{12}C reaction at 90.5, 110 and 130 MeV beam energy**, University of Bologna, 2017.

[16] A. Boschi, **Bachelor Thesis: Misure di reazioni di fusione-evaporazione ^{16}O + ^{12}C. Risultati Preliminari**, University of Bologna, 2016.

[17] L. Morelli *et al.*, **Nucl. Instr. and Meth. A 620, 305**, 2010.

[18] A. Camaiani, **Master Thesis: Study and decays reconstruction of ^{25}Mg system formed in ^{12}C + ^{13}C reaction at 95 MeV as a way to highlight possible structural effects**, University of Florence, 2016.

[19] G.F. Knoll, **Radiation Detection and measurements**, ed. John Wiley and Sons, New York, 1989.

[20] ROOT Data Analysis Framework: https://root.cern.ch/

[21] NUDAT2 online database: http://www.nndc.bnl.gov/nudat2/

[22] NUCL-EX Collaboration INFN: http://www.bo.infn.it/nucl-ex/

[23] R.J. Charity *et. al.*, **Phys. Rev. C 46, 1951**, 1992.

[24] T. Giammaria, **Bachelor Thesis: Decadimento del ^{12}C eccitato in reazioni ^{12}C + ^{12}C: Stato eccitato di Hoyle**, University of Bologna, 2015.

[25] J.L. Basdevant, J. Rich and M. Spiro, **Fundamentals In Nuclear Physics. From Nuclear Structur e to Cosmology**, ed. Springer, 2005.

Ringraziamenti

Desidero ringraziare, innanzitutto, il professor Mauro Bruno per la disponibilità, l'attenzione e la gentilezza dimostrate durante il percorso che ha portato alla stesura di questa tesi. Sono stata fortunata ad avere una guida tanto valida e preziosa. Un immenso grazie va al dottor Catalin Frosin, che stimo molto e che reputo una persona in gamba e brillante, per avermi guidato e insegnato con tanta pazienza. Che tu possa avere sempre il vento in poppa e raggiungere i tuoi grandi obiettivi. Ringrazio la mia famiglia per avermi permesso di percorrere e concludere con serenità e con le spalle ben coperte questo faticoso ma entusiasmante cammino. Ringrazio soprattutto mia madre, alla quale dedico questa tesi, che per me non è solo una mamma affettuosa, ma anche e soprattutto una straordinaria amica. Non basterebbe di certo dare anche a lei una corona d'alloro per ringraziarla per il supporto dimostratomi e, di sicuro, non bastano queste poche righe per dirle quanto io le sia grata per ciò che fa per me tutti i giorni. Ringrazio tutti i miei amici, dalle amicizie storiche a quelle più recenti fatte durante questa avventura accademica e le mie fantastiche coinquiline. Senza di voi mi sentirei persa. Infine, ringrazio Leonardo per essermi stato accanto con pazienza e per avermi sempre incoraggiata e fatto ridere anche nei momenti più bui. Grazie.